Numerical study on the structural response of a masonry arch bridge subject to flood flow and debris impact

Eda Majtan [a,b*], Lee S. Cunningham [a] and Benedict D. Rogers [a]

[a] Department of Mechanical, Aerospace and Civil Engineering, The University of Manchester, Manchester, M13 9PL, UK.
[b] School of Science, Engineering and Environment, University of Salford, Manchester, M5 4WT, UK
*Corresponding author. Email: e.majtan@salford.ac.uk

Abstract

Extreme flood flows in rivers and the floating debris they carry have the potential to generate significant impact forces on bridges spanning the watercourse. Recent flood events have highlighted the vulnerability of masonry arch bridges in flood events. This paper explores the structural response of a typical masonry arch bridge subject to flood flow and impact from flood-borne debris using a validated numerical modelling approach. The meshless method smoothed particle hydrodynamics (SPH) is used to model the fluid behaviour giving the pressure distributions on a single-span arch bridge arising from both the fluid and debris impact. Taking the pressure-time histories derived from the SPH model, the response of the bridge structure is then simulated using a nonlinear finite element (FE) model via Abaqus/Explicit. The effects of submergence ratio of bridge components: abutment, arch barrel, spandrel wall, debris orientation and flow velocity are explored. Results indicate that the debris impact resulted in greatest increase in the stresses in the bridge with a fully submerged abutment and side-on (0-degree) debris orientation. The influence of the debris impact with end-on (90-degree) orientation on the structural response was relatively low despite its higher peak pressure values. Moreover, for the type of realistic flow scenarios considered, significant local tensile stresses can be generated in the spandrel wall and arch barrel leading to structural damage.

Keywords: Masonry arch bridges, flood effects, hydrodynamic force, debris impact, buoyancy effect, finite elements, smoothed particle hydrodynamics, DualSPHysics

1. Introduction

Masonry arch bridges are among the oldest bridge forms in use and continue to play a vital role in the transport networks in many locations around the world. It is estimated that between 200,000 and 500,000 masonry arch bridges are in daily use in mainland Europe [1] with approximately 40,000 in the UK, corresponding to ~40% of the total bridge stock [2]. Although these structures have typically demonstrated good performance under normal service loads, increased frequency and intensity of extreme environmental loading such as flash flooding etc., present a major challenge to their long-term viability. Failure and damage of masonry arch bridges result in not only disruption to transportation networks and communities, but also economic losses owing to the cost of remedial works and bridge replacement, and most importantly may result in loss of life [3].

Table 1: Details of several flooded masonry arch bridges in the UK (2009-2021)

Bridge name	Area	No of Spans	Date of flooding	Flood effect on the bridges	Damage source	Debris types
Workington (Calva)	Workington	3	2009	Partially collapsed	S, F, D	Tree log
Northside	Workington	3	2009	Bridge collapsed	F	-
Little Braithwaite	Braithwaite	1	2009, 2015	Bridge collapsed in 2009, partially collapsed in 2015	F, D	Tree log
Coledale High	Braithwaite	1	2015	Parapet collapsed	F,D	Tree log
Bell	Welton	1	2015	Bridge collapsed	S,F	-
Pooley	Ullswater	3	2009, 2015	Damaged in 2009, bridge collapsed in 2015	S,F	-
Waterstave Bridge	Bradninch	1	2012	Bridge collapsed	F	-
Eamont	Penrith	3	2015	Damaged	S	Asphalt portion
Brougham Castle (Old)	Penrith	3	2015	Partially collapsed	S,F	Small boulders
Sprint	Burneside	1	2015	Damaged	S,F	-
Tadcaster	N. Yorks	9	2015	Partially collapsed	S,F	-
Ballynameen	Claudy	5	2017	Partially collapsed	F	-
Cogden South (Grinton Moor)	N. Yorks	1	2019	Bridge collapsed	F	-
Llanerch Bridge	Denbighshire	1	2021	Bridge collapsed	F	-

Note: Damage sources: S = scour; F = flood; and D = debris impact defined according to the study of Deng et al. [4]. All data collected from published resources[5–20], details e.g. hydraulic data at the bridge locations, bridge dimensions, debris details etc. are required for further investigations.

Masonry arch bridges spanning watercourses are vulnerable to flood-induced loads that can cause serious structural damage. Notable examples include the bridges damaged by recent extreme events such as storm Desmond and Eva in the UK in December 2015 [16]. Over the last two decades, a significant amount of masonry arch bridges in the UK have incurred failure or serious damage resulting from extreme flood events as detailed in Table 1. In all of these cases, the masonry constituted stone blockwork with the exception of Waterstave Bridge which was of clay brickwork construction. The sources of bridge failures or damages were classified in accordance with Deng et al. [4] as scour, i.e. undermining of the bridge foundation due to removal of sediment (S), flood damage to the bridge superstructure from the hydrodynamic action of the flow (F) and debris impact (D) from flood-borne objects such as tree logs. A debris-induced damage or failure has been designated only where categorically stated, in many other cases debris was cited as being present without the being directly attributed to the failure e.g. Tadcaster Bridge as discussed by the Institution of Civil Engineers [19].

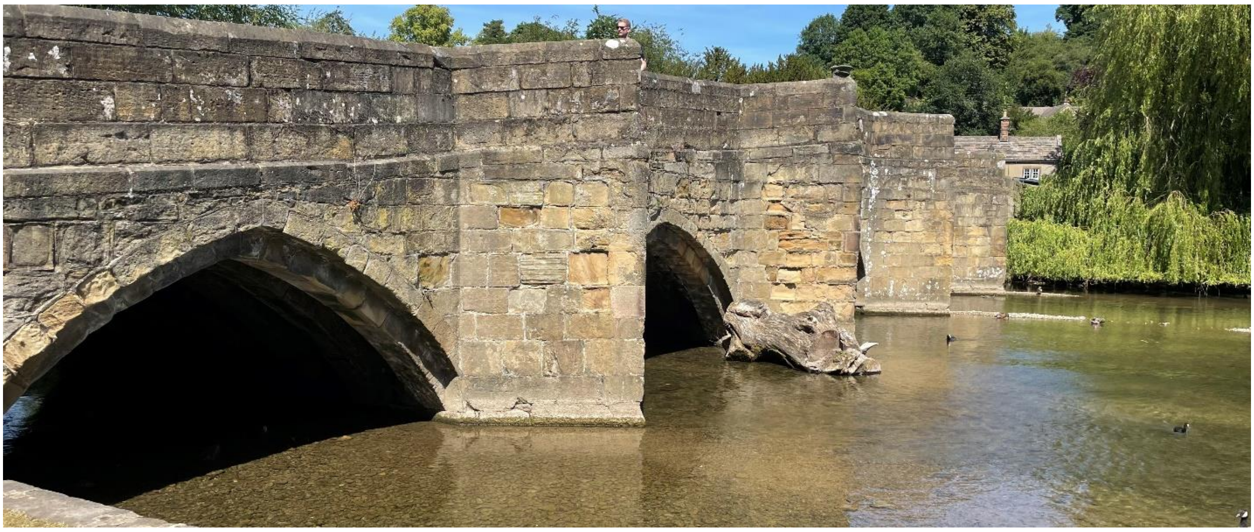

Fig. 1: Woody debris (tree trunk) around Bakewell Bridge spanning the River Wye in Bakewell, Derbyshire, UK (Image by Eda Majtan)

The flood-induced forces exerted on a masonry arch bridge comprise horizontal hydrostatic forces, hydrodynamic drag and uplift forces, hydrostatic uplift or buoyancy forces where components are submerged and also floating debris impact forces. Depending on the flow velocity, hydrodynamic forces can result in serious damage, particularly when the buoyancy forces reduce the effective self-weight of submerged main structural components such as the arch barrel and associated fill. In addition to this, the presence of the debris inside the flow as shown in Fig. 1 results in increases in water level corresponding to an increase in both hydrostatic and hydrodynamic forces as well as the debris impact force itself on the structural members including the abutment, spandrel wall and arch barrel [21]. Existing research has tended to focus on scour effects on bridge abutments during flooding. Despite its destructive potential, the interaction between the arch superstructure, flood flows and debris, has received relatively little attention. [22].

Most existing masonry arch bridges were built before the early 1900s without consideration of flood-induced loads. Although the UK bridge assessment code CS 469, formerly BD 97/12 [23,24] and Ciria C742 [25] present evaluation methods for hydraulic actions at existing highway bridges, the focus is on scour rather than any direct effects on the bridge superstructure. The Highways England design code CD 356 [26] addresses hydraulic actions on bridge piers considering the length-to-width ratio, in addition to the actions on the submerged superstructure by suggesting drag coefficients for a typical rectangular deck, however, no detailed provision is made for debris impact. A detailed study described by the US NCHRP Report 445 [27] was performed to develop equations for estimating the maximum waterborne debris forces on bridge piers and superstructures including changes in drag coefficient in relation to the flow-blockage ratio with different Froude numbers. However, the bridge types investigated in the aforementioned report were simple beam bridges in either steel or concrete. To investigate the reduction in the load carrying capacity of fully submerged masonry arch bridges due to the resulting buoyancy forces, Hulet et al. [28] conducted small-scale experiments considering three flooding scenarios and a reference case: (a) a dry bridge, (b) an unwaterproofed bridge, (c) a waterproofed bridge with external flooding and dry backfill and (d) a waterproofed bridge with internal flooding and saturated backfill. Despite the same failure type, i.e., a four-hinge mechanism, being observed in all bridges under vertical load, the study found that a significant reduction in the load carrying capacity of the bridges occurred where the arch barrel was submerged, 40% in scenario (b) and

43% in scenario (c). The load carrying capacity slightly increased in scenario (d) owing to the greater weight of saturated backfill material adopted. Proske et al. [22] performed a 1:20 scale experiment to determine the load carrying capacity of a masonry arch bridge subject to horizontal static and dynamic forces in the transverse direction, i.e. perpendicular to the bridge span, representing debris flow containing a large amount of sediment and debris inside the flow, e.g. a boulder based on their field measurements. The study revealed different failure modes of the arch barrel under static and dynamic loads, most importantly the greatest structural damage occurred in the case of debris impact. Although Proske et al. [22] postulated that flood-induced transient horizontal loads might cause failure of a spandrel wall e.g. sliding, bulging and rotation of spandrel walls [29] and thus failure of the bridge, there is a scarcity of studies on the behaviour of masonry arch bridges subject to flood induced hydrodynamic and impact forces.

One of the reasons for the scarcity in such studies is the difficulty in accurately obtaining the force-time histories associated with these events. Experimental studies may be limited by the method of data capture e.g. uncertainty in the location of peak pressure and hence pressure probe location. This problem may be overcome by numerical modelling. Various mesh-based computational fluid dynamics (CFD) approaches have been used to estimate the hydrodynamic loading on an obstacle, e.g. pier, or other bridge forms, these methods have included the finite difference method (FDM) [30], the finite element method (FEM) [31] and the finite volume method (FVM) [31–33] by applying a volume-of-fluid (VOF) method to track the free surface.

Modelling free-surface flow carrying moving debris around a bridge including both fluid-solid and solid-solid interactions can be a significant challenge for these mesh-based methods [34]. An alternative to these is the meshless method of smoothed particle hydrodynamics (SPH). The basis of the SPH method for fluid mechanics is the solution of the Navier-Stokes equations using a Lagrangian approach. In the SPH method, the flow is represented with moving particles where physical properties of the flow are carried with each particle. SPH has the capability to simulate engineering problems including fast-dynamic flows, large deformations of the fluid domain with a complex free surface, motions of a floating body and the interfaces between fluid-solid as well as solid-solid regions [35]. This is in contrast to other aforementioned CFD methods which require a special treatment, such as VOF, to track the free surface and moving floating debris with high computational cost associated by the remeshing technique [36,37].

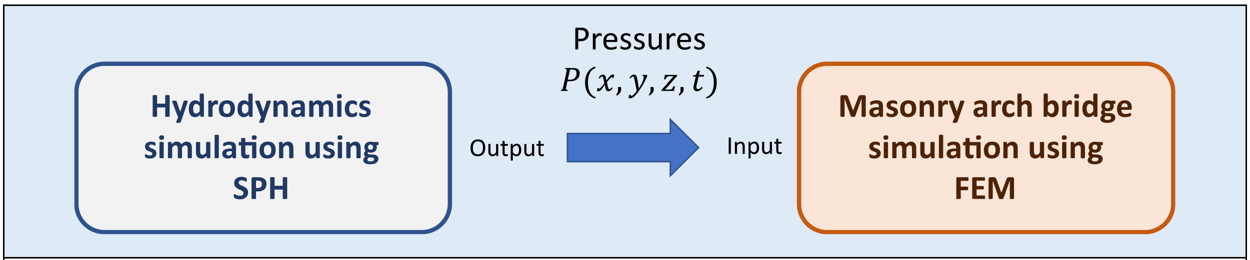

Fig. 2: One-way coupling approach for combined modelling of hydrodynamics and structural response of masonry arch bridge

Recent developments in fluid-structure interaction problems have seen SPH models coupled with other methods such as the discrete element method (DEM) or FEM [38–40] to achieve two-way coupling. In two-way coupling, the deformation of the structure and its effect on the hydrodynamics of the fluid is simulated, however such approaches can be computationally expensive. This issue is compounded when accounting for the complex nonlinear behaviour of the masonry arch bridge [41] and where 3D modelling of the fluid and the structure is necessary. Whilst two-way coupling may be useful where the impacted structure is comparatively flexible, in the case of an essentially rigid structure such as a masonry arch bridge, where anticipated deflections are minimal, a one-way coupling approach can be justified. In one-way coupling, the hydrodynamic model is used to derive the pressures acting on the structure assuming it to be rigid, these pressure-time histories are then used as the input to a separate bridge model incorporating realistic material models (Fig. 2). The work presented here adopts the one-way coupling approach using SPH in combination with the FEM considering the main aim of the research, investigating the global behaviour of the bridge subject to flood-induced loads. In cases where the local behaviour is of key interest, a micro-modelling approach can be used or alternatively a discrete element method approach (DEM) [42,43]. The SPH simulations were conducted using the open-source code, DualSPHysics version 4.4 [44,45], while the FE work employed the software

Abaqus/Explicit 2020. The flood-induced loads on a scale model bridge were investigated in the SPH simulations since this paper presents part of authors' wider study involving laboratory experiments using a scale model of the representative masonry arch bridge [46]. After a Froude scaling law was applied to the pressure-time histories obtained from the model bridge, the structural response of the corresponding full-scale arch bridge was obtained via FE analysis. It should be noted that the full-scale density of the bridge material was also adopted in the scaled down model. Since the entire bridge structure was simulated, a macro-modelling approach was adopted for the FE analysis of the masonry for computational efficiency [47–50].

The structure of the paper is as follows. Firstly, a brief explanation of the SPH method is presented followed by use of a validated SPH model to simulate flood-induced flow and debris impact on the representative 1:10 scale bridge. Next, the FE model used in this study is validated and then deployed to evaluate the structural response of the full-scale bridge to the pressure-time histories obtained from the SPH simulations. Finally, the implications of the numerical results are discussed and future work is identified.

2. Investigation of flood-induced forces on a single-span masonry arch bridge

Considering the scope of this present research, a brief explanation of the SPH method is first provided. Further information and detailed validation studies of the SPH method for the hydrodynamics and the floating debris striking a bridge can be found in the previous authors' study, Majtan et al. [51]. The flood-induced forces on a single-span masonry arch bridge (1:10 scale) with different submergence ratios of its structural components, abutment, arch barrel and spandrel wall, and orientations of floating debris impacts are investigated herein.

2.1. Overview of smoothed particle hydrodynamics (SPH) method

SPH solves the Navier-Stokes equations in Lagrangian form where the fluid is represented by a set of moving particles carrying physical properties, e.g., density, velocity and pressure. These properties are updated at every time step according to its neighbouring particles via use of an SPH discretisation for integral interpolants. An in-depth presentation of the SPH methodology can be found in Violeau and Rogers [35] and full details of the weakly compressible SPH formulation used in this paper is presented in Domínguez et al. [45]. Herein, only the main equations are presented. The Navier-Stokes equation for mass and momentum conservation in Lagrangian form are:

$$\frac{d\rho}{dt} = -\rho\nabla.\boldsymbol{v} \tag{1}$$

$$\frac{d\boldsymbol{v}}{dt} = -\frac{1}{\rho}\nabla P + \upsilon_0 \nabla^{\boldsymbol{2}}\boldsymbol{v} + \boldsymbol{g} \tag{2}$$

where ρ is the density, t is the time, $\boldsymbol{v}$ is the velocity vector, P and υ_0 denote the pressure and kinetic viscosity (10^{-6} m^2s^{-1} for water), while $\boldsymbol{g}$ represents the gravitational acceleration (0, 0, -9.81 m s^{-2}). The integral form of Eq. (1) is rewritten for an interpolated particle a in SPH discrete form considering the effect of each neighbouring particle b as:

$$\frac{d\rho_a}{dt} = \rho_a \sum_b (\boldsymbol{v}_a - \boldsymbol{v}_b) \cdot \nabla_a W_{ab} \frac{m_b}{\rho_b} \tag{3}$$

where m_b and ρ_b represent the mass and density of particles b, $\nabla_a W_{ab}$ is the gradient of the smoothing kernel, W_{ab}, with respect to particle a. The smoothing kernel, W_{ab}, is obtained based on the distance between particles a and b and the smoothing length (h). In the SPH discretisation, the form of the kernel function W_{ab} can be chosen based on desired accuracy and computational cost; the fifth-order Wendland kernel is chosen for this research [45].

There are two different viscosity treatments available in DualSPHysics for the momentum equation: (i) artificial viscosity or (ii) laminar + sub-particle stress (SPS) turbulence methods including an empirical value and real viscosity for water, respectively. Following previous validation by the authors [51], this study uses the second method which is based on a large-eddy simulation (LES) approach for WCSPH. Thus, the momentum equation in SPH form with laminar+SPS treatment is given:

$$\frac{d\boldsymbol{v}_a}{dt} = -\sum_b m_b \left(\frac{P_a + P_b}{\rho_a\,\rho_b}\right) \nabla_a W_{ab} + \boldsymbol{g} + \sum_b m_b \left(\frac{4\,\upsilon_0\,\boldsymbol{r}_{ab}\cdot\nabla_a W_{ab}}{(\rho_a+\rho_b)(r_{ab}^2+\eta^2)}\right)\boldsymbol{v}_{ab} + \sum_b m_b \left(\frac{\overrightarrow{\tau_a^{ij}} + \overrightarrow{\tau_b^{ij}}}{\rho_a\,\rho_b}\right)\nabla_a W_{ab} \tag{4}$$

where $\overrightarrow{\tau^{ij}}$ is the sub-particle stress (SPS) tensor and $\eta = 0.01h^2$ [52]. It should be also noted that although two SPH formulations are used by SPH solvers, incompressible SPH (ISPH) [53] and weakly compressible SPH (WCSPH) first proposed by Monaghan [54], this study employs WCSPH via use of DualSPHysics owing to its accurate results for fluid-structure interactions without any fluctuation problems in pressure [55–57].

2.2. SPH modelling and results of 1:10 scale bridge

This present paper is part of a wider research campaign including experimental works in the laboratory flume at the University of Manchester, UK [46]. In the SPH numerical simulations, a model arch bridge of 1:10 scale was therefore used to match the physical flume dimensions. The geometry of a representative masonry arch bridge was proportioned in accordance with dimensions of typical masonry arch bridges in the field, see Table 2. The representative full-scale bridge consisted of 8 m span, 0.25 rise-to-span ratio and 4 m width in the streamwise direction in consideration of a single vehicular lane bridge. At the 1:10 scale model bridge, these dimensions correspond to 0.8 m span and 0.4 m width shown in Fig. 3(a) and Fig. 3(b). Following the particle convergence studies published previously by the authors [51], an initial inter-particle distance of d_p = 0.01 m was chosen.

Table 2: Geometrical properties of masonry arch bridge[58–61]

Bridge Name	Span (m)	Rise (m)	Rise/ span	Bridge width (m)	Arch thickness (m)	Spandrel wall thickness (m)	Backfill depth at crown (m)
Torksey	4.90	1.15	0.23	7.80	0.343	0.380	0.246
Bridge 270	2.70	1.35	0.50	2.00	0.350	0.480	0.750
Dundee	4.00	2.00	0.50	6.00	0.250	0.330	0.250
Bolton	6.00	1.00	0.17	6.00	0.220	0.660	0.300
Prestwood	6.55	1.43	0.22	3.80	0.220	0.380	0.165
Shinafoot	6.16	1.18	0.19	7.20	0.390	0.370	0.215
Strathmashie	9.42	2.99	0.32	5.81	0.600	0.400	0.410

Bridgemill	18.30	2.85	0.16	8.30	0.711	0.500	0.200
Jones	6.88	2.62	0.38	5.79	0.460	-	0.300
Oberlin	6.10	2.59	0.42	8.79	-	-	0.300
Kimbotlon B.	8.00	2.00	0.25	10.00	0.440	0.500	0.400
Temple	3.00	0.68	0.23	6.53	0.380	-	0.050
Oghermong UB	7.80	2.00	0.26	3.60	0.550	-	0.120
Owenmore UB	8.60	2.28	0.27	3.82	0.440	-	0.320
Windy	10.70	1.97	0.18	4.05	0.670	-	0.300
Killeen	9.30	2.65	0.28	3.15	0.446	-	0.126

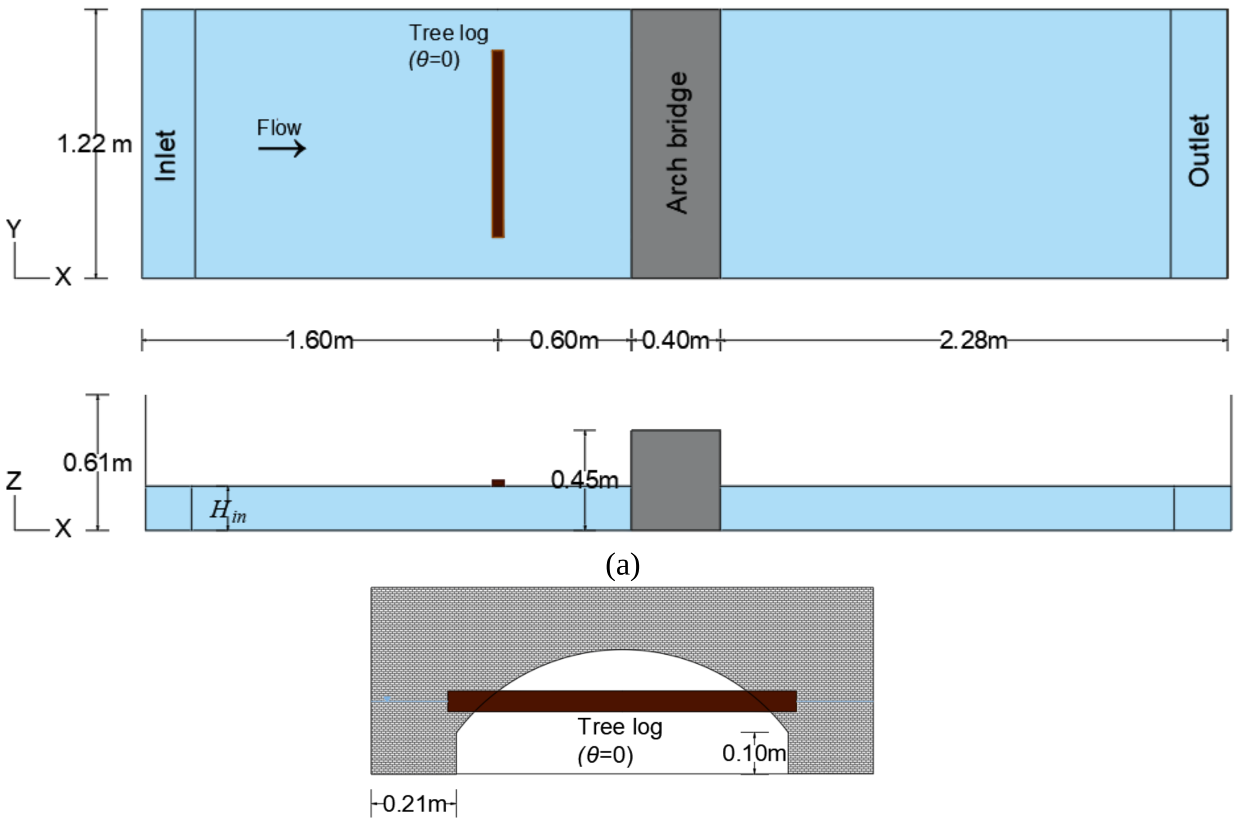

(b)

Fig. 3: (a) Plan and side view of the numerical domain (b) a single-span arch bridge with the 0-degree initially oriented tree log (not to scale)

The hydraulic conditions were defined considering the flume capacity. Three hydraulic conditions in relation to submergence ratio of the structural components, abutment, arch barrel and spandrel wall were examined keeping the velocity of the free surface at 0.2 m/s with two debris orientations (θ) for its initial position (Table 3). The most common significant debris type in a natural watercourse, a floating tree log, was simulated in the present investigation. Using data from previous studies [62–64], the log's diameter-to-length ratio was chosen as 0.059 (Fig. 3(b)). The source wood for tree log was specified as English Brown Oak which has a density of 740 kg/m^3 [65]. The 0-degree and 90-degree initial debris orientations represented a side-on and end-on impact i.e., where the log's long axis was parallel and perpendicular to the bridge span respectively. Note that due to the flume capacity, a relatively slow flow was examined herein with the free-surface velocity of 0.2 m/s at the inlet, corresponding to a Froude number of 0.071 in case 1, 0.059 in case 2 and 0.051 in case 3. This corresponds to 0.63 m/s at the prototype scale. The field data from a real-life flooding scenario is discussed in Section 3.3.3

Table 3: Scenarios for submergence ratio of structural components and debris details

Case No.	Flow depth at inlet, H_{in} (m)	Flow rate (m^3/s)	Fully submerged structural component	Debris	Debris length (m)	Debris diameter (m)	Initial debris orientation (degrees)
1	0.2	0.0242	Abutment	-	-	-	-
1A	0.2	0.0242	Abutment	Tree log	0.84	0.05	0
1B	0.2	0.0242	Abutment	Tree log	0.84	0.05	90
2	0.3	0.0363	Arch barrel	-	-	-	-
2A	0.3	0.0363	Arch barrel	Tree log	0.84	0.05	0
2B	0.3	0.0363	Arch barrel	Tree log	0.84	0.05	90
3	0.4	0.0484	Spandrel wall	-	-	-	-
3A	0.4	0.0484	Spandrel wall	Tree log	0.84	0.05	0
3B	0.4	0.0484	Spandrel wall	Tree log	0.84	0.05	90

Fig. 4(a), Fig. 4(d) and Fig. 4(g) illustrate the pressure distribution on the 1:10 scale bridge when the abutment, arch barrel and spandrel wall were submerged corresponding to case 1, 2 and 3 in Table 3, respectively. The flow was modelled over a 10-second period, the impact events occurring between 6 s and 10 s are investigated herein. Fig. 4(b) and Fig. 4(c) show average pressure histories obtained on the back and front spandrel walls in case 1 where the measurements points are given in Table 4. Similarly, Fig. 4(e) and Fig. 4(f) are for case 2 and Fig. 4(h) and Fig. 4(i) for case 3. It should be reiterated that these pressure-time histories pertain to the 1:10 scale bridge. In accordance with Froude scaling [66], these pressures were multiplied by a factor of 10 before being applied to the full-scale FE model of the bridge presented later.

Table 4: Measurement points at back and front walls in case 1, 2 and 3

	Back (B)		Front (F)	
	Name	Measurement point (x,y,z)	Name	Measurement point (x,y,z)
Case 1	BL1	2.63, 0.2, 0.03	FL1	2.17, 0.2, 0.03
	BL2	2.63, 0.2, 0.08	FL2	2.17, 0.2, 0.08
	BL3	2.63, 0.2, 0.13	FL3	2.17, 0.2, 0.13
	BL4	2.63, 0.2, 0.18	FL4	2.17, 0.2, 0.18

Case 2	BL1	2.63, 0.2, 0.03	FL1	2.17, 0.2, 0.03
	BL2	2.63, 0.2, 0.08	FL2	2.17, 0.2, 0.08
	BL3	2.63, 0.2, 0.13	FL3	2.17, 0.2, 0.13
	BL4	2.63, 0.2, 0.18	FL4	2.17, 0.2, 0.18
	BL5	2.63, 0.2, 0.23	FL5	2.17, 0.2, 0.23
	BL6	2.63, 0.2, 0.28	FL6	2.17, 0.2, 0.28
Case 3	BL1	2.63, 0.2, 0.03	FL1	2.17, 0.2, 0.03
	BL2	2.63, 0.2, 0.08	FL2	2.17, 0.2, 0.08
	BL3	2.63, 0.2, 0.13	FL3	2.17, 0.2, 0.13
	BL4	2.63, 0.2, 0.18	FL4	2.17, 0.2, 0.18
	BL5	2.63, 0.2, 0.23	FL5	2.17, 0.2, 0.23
	BL6	2.63, 0.2, 0.28	FL6	2.17, 0.2, 0.28
	BL7	2.63, 0.2, 0.33	FL7	2.17, 0.2, 0.33
	BL8	2.63, 0.2, 0.38	FL8	2.17, 0.2, 0.38

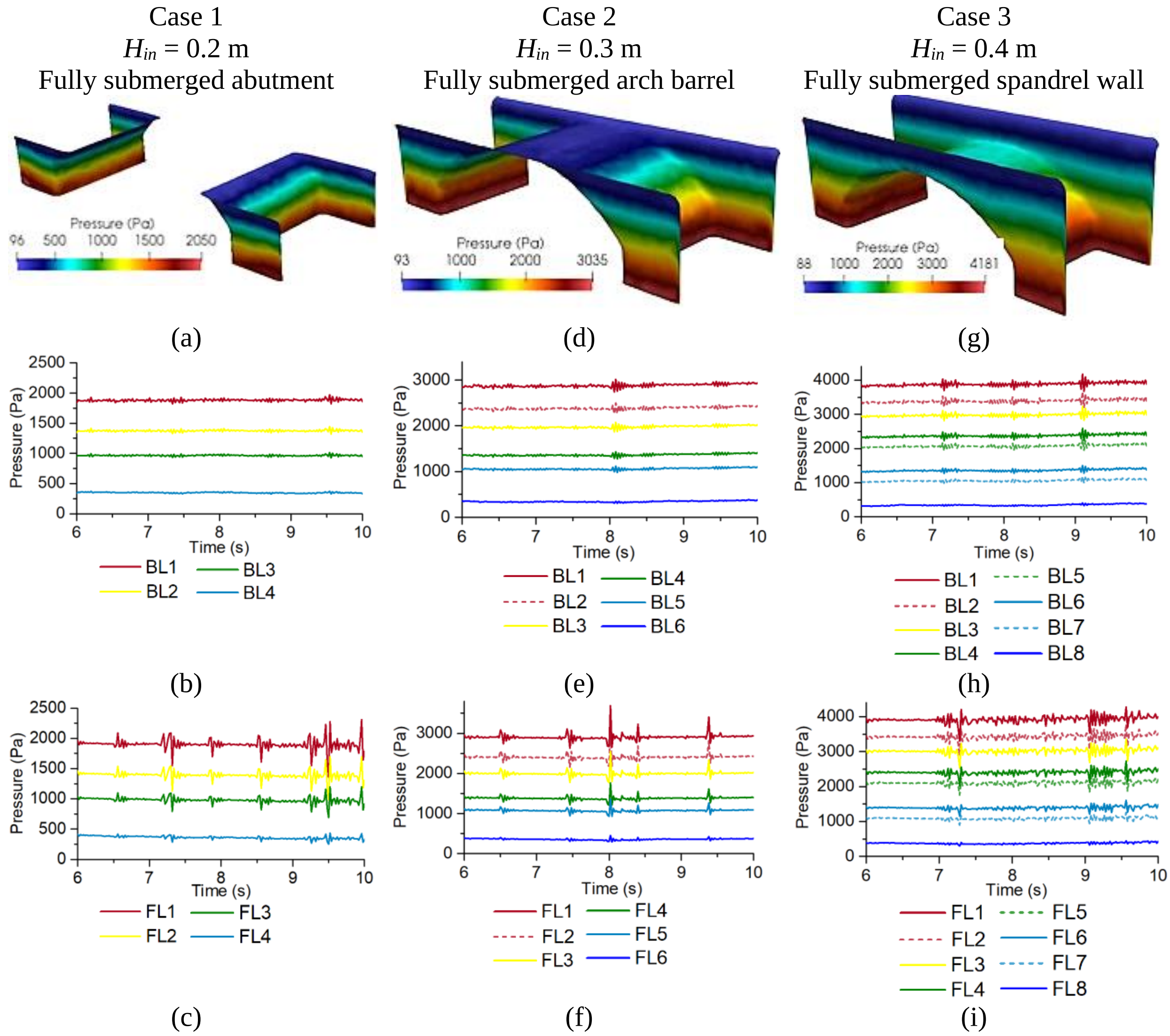

Fig. 4: Pressure distribution from SPH simulations on 1:10 scale bridge (a) case 1, (d) case 2 and (g) case 3 and pressure-time histories on back and front walls (b, c) case 1, (e, f) case 2 and (h, i) case 3

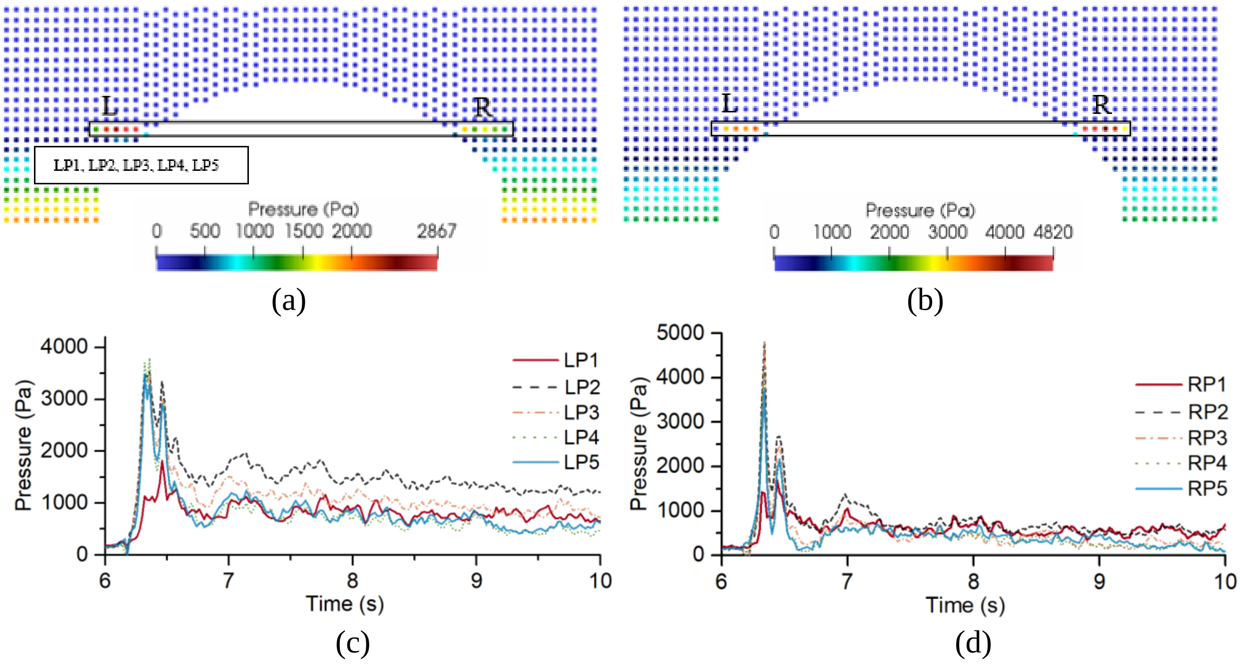

Fig. 5: Case 1A (a) combination of hydrodynamic and debris impact pressure distribution at the first debris impact, t = 6.28 s, and (b) peak debris impact values , t = 6.32 s, where the debris impact locations were shown at the left (L) and right (R) side of the bridge (c) pressure-time histories at peak debris impact locations at L with LP1-LP5, (d) pressure-time histories at peak debris impact locations at R with RP1-RP5 in the order from outside to inside

To map the debris impact pressures on the faces of the front spandrel wall and abutment a grid of numerical pressure probes with a separation of 0.02 m were used as shown in Fig. 5(a) and Fig. 5(b). The debris impact pressures decreased with the increase in the water depth H due to decrease in the debris velocity, thus the number of numerical pressure probes in contact with the debris depends on distinct debris impact pressures captured when the debris strikes the bridge structure. Herein, (i) LP and RP are used to refer to the left- and right-hand sides of the upstream bridge face impacted by the debris; and (ii) the numbers 1-5 indicate the numerical pressure probe impacted with 1 being the furthest from the arch barrel and 5 being nearest the arch barrel, see Fig. 5(a). Fig. 5(a) shows the pressure distribution on the spandrel wall at the first debris impact, t = 6.28 s in case 1A, while Fig. 5(b) gives peak pressure values associated with the debris impact at t = 6.32 s. Fig. 5(c) and Fig. 5(d) provide detailed pressure-time histories where the debris impacted the left (L) and right (R) side of the bridge in the order from outside to inside.

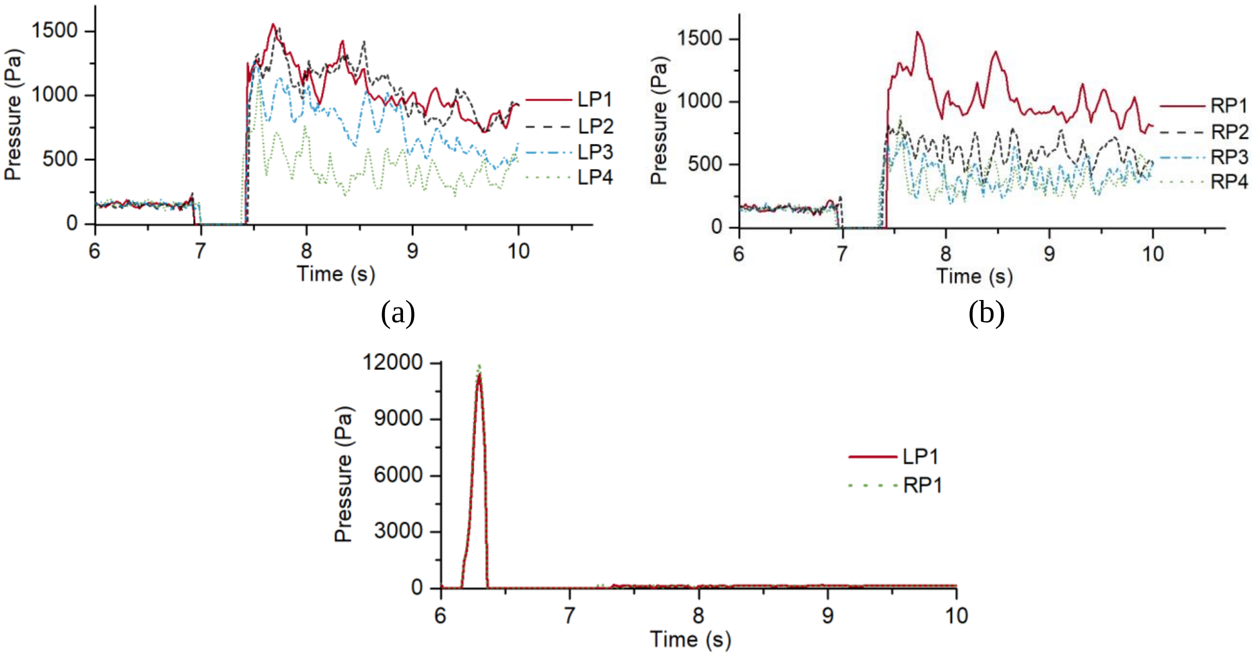

(a) (b)

(c)

Fig. 6: Pressure-time histories associated with the debris impact on (a) left (L) and (b) right (R) sides of the bridge in case 2A, (c) both left and right side of the bridge in case 2B

In case 1B, the initially 90-degree oriented debris was transported without impacting the bridge. Similar to case 1A, the left and right sides of the bridge were used to provide detailed pressure-time histories in case 2A, Fig. 6(a) and Fig. 6(b) and in case 2B, Fig. 6(c). It can be seen that when the arch barrel was submerged, less debris impact load was observed on the bridge in case 2A (Fig. 6(a)) compared to case 1A with 0-degree initial debris orientation (Fig.5(a)-(d)), while the debris orientation of 90 degree in case 2B (Fig.6(c)) led to increases in the peak impact ~7.5 times higher than that in case 2A (Fig. 6(a)) with shorter rise time, 0.12 s.

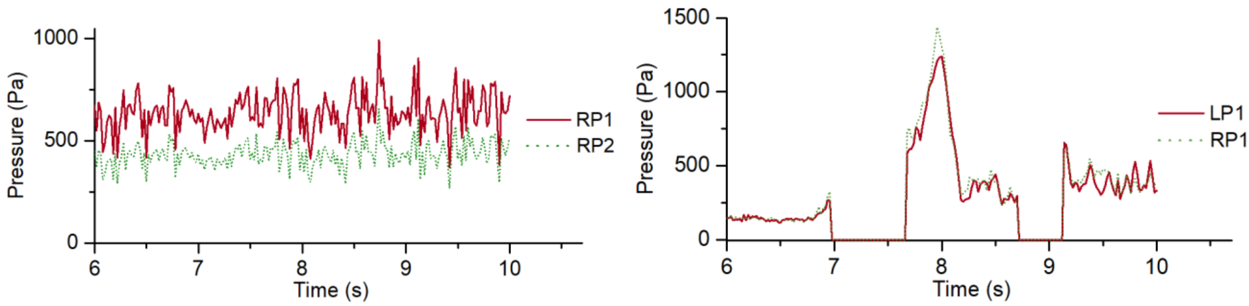

(a) (b)

Fig. 7: Pressure-time histories associated with the debris impact in (a) case 3A and (b) case 3B

The pressure-time histories at the impact locations are provided in Fig. 7(a) and Fig. 7(b) for case 3A and case 3B, respectively. When the spandrel wall was fully submerged, the flow fluctuation in front of the bridge resulted in rotation of the debris leading to an oblique impact in case 3A, whilst the same angle as its initial condition was observed in case 3B.

3. FE modelling of the full-scale masonry arch bridge

The structural analysis of masonry is complex due to its non-homogeneous and anisotropic nature. There are three main approaches to FE modelling of masonry, each with implications for accuracy and computational efficiency, these are detailed micro-modelling, simplified micro-modelling and macro-modelling. In the detailed micro-modelling approach, the masonry unit and mortar are modelled as a continuum element and the interface between them as a discontinuum element, while in the simplified micro-modelling approach the units are expanded and the interface between them is assigned based on the mortar properties. Macro-modelling assumes the masonry to be a homogenous continuum without direct consideration of the interface between units and mortar and is used where the global behaviour of the whole structure is of interest [47,67–69]. Many existing studies have focused on the behaviour of the masonry arch barrel itself under vertical loading using mesoscale modelling approaches including simplified micro-modelling of the arch barrel and macro-modelling of the spandrel walls and backfill without consideration of the transverse behaviour of the bridge [70,71]. Since the present study seeks to investigate the global behaviour of the entire bridge, a macro-modelling approach for all structural components is adopted [48,58,61] with a focus of brickwork masonry. In the forthcoming section, a brief description of the methodology used in this study is detailed. The macro-model approach is first validated using experimental data of brickwork walls subject to out-of-plane impact. Following this, the validated modelling approach is used to investigate the behaviour of a representative single-span masonry arch bridge under different flooding scenarios.

3.1. Background to FE modelling approach

Hydrodynamic and debris impact loads are time-dependent dynamic loads; hence an explicit solver was employed in this work due to its numerical stability in such applications [47,56]. All models used 3-D solid 8-node hexahedral elements (C3D8R) with linear, first order, interpolation. These elements accommodate a reduced integration technique and hourglass control to tackle possible uncontrolled distortion of the mesh. To optimise the model in terms of accuracy and computational efficiency as well as tackle mesh distortion in the masonry arch bridge models, an adaptive mesh refinement was also performed by reducing the element size locally.

To model the nonlinear behaviour of masonry, the concrete damaged plasticity (CDP) model was chosen due to its suitability for quasi brittle materials in compression and tension [72]. The CDP model can be employed by defining the plasticity parameters, compressive behaviour and tensile behaviour of the material. In the plasticity parameters, the dilation angle (ψ) is the internal friction of the material representing the angle of the plastic potential function ranging between 12 and 37 degrees depending on the roughness of the unit surfaces. While lower values were used for the brick masonry walls by Cavaleri et al. (2020) [47], the dilation angle was kept between 24 and 37 in previous studies of masonry arch bridges with both brick and stone masonry [58,59,70]. It should be noted that using lower dilation angle values due to less friction might lead to a decrease in the structure's stiffness. ϵ is the flow potential eccentricity and f_{b0}/f_{c0} is the ratio of initial compressive yield stresses under biaxial and uniaxial loads with the default values of 0.1 and 1.16, respectively [73]. K_c represents the ratio of the second stress invariants on the tensile meridian to the compressive meridian at the yield surfaces that ranges between 0.5 and 1.0 with the default value of 0.67 [73]. The viscosity parameter, μ, is a viscoplastic regularisation used to tackle convergence problems during stiffness degradation and softening behaviour of the material, particularly in Abaqus/Standard with an implicit scheme [73,74]. The present work adopts a value of $\mu = 0$ since the convergence problems pertain to the implicit regime and not explicit.

Masonry is a non-homogeneous and anisotropic material consisting of stiffer units and softer mortar. Masonry typically has higher resistance to compressive forces and very low resistance in tension due in part to the weak bond between unit and mortar. If the brick and mortar types used in the masonry assembly are known, design codes such as BS 5628 [75] and Eurocode 6 [76] present equations to predict the compressive, shear and tensile strength of the masonry assembly.

Current design codes deal with modern units and mortar types, whereas most masonry arch bridges are of historic construction. In the case of assessment of existing masonry bridges, Hendry [49] found that BS 5628 provides a better agreement with the experimental results compared to Eurocode 6. The study of Kaushik et al. [77] found that the Eurocode 6 overestimates the compressive strength for brick masonry according to their experimental results and proposed a modification to the Eurocode 6 equation as follows:

$$f_c = 0.63\, f_b^{0.49}\, f_m^{0.32} \tag{5}$$

where f_c is the compressive strength of masonry assembly and f_b and f_m represent the compressive strength of brick unit and mortar, respectively. The proposed equation may underestimate the compressive strengths of brickwork with relatively high compressive strength of brick reported by Hendry [49], however the tests results from other existing masonry arch bridges [78,79] were well predicted. In the present study, Eq. 5 was employed for the numerical model where the unit and mortar strength are known. Kaushik et.al [77] also provided the compressive stress-strain relationship for brick masonry with different mortar types where the peak strain, ε_c, and the elastic modulus, E_c, can be calculated:

$$\varepsilon_c = \frac{0.27}{f_m^{0.25}} \frac{f_c}{E_c^{0.7}} \tag{6}$$

$$E_c = 550 f_c \tag{7}$$

Like Eq. 7, many studies in the literature suggested using the multiplier of 550 [47,49] compared to the multiplier of 1000 and 900 proposed by Eurocode 6 and BS 5628, respectively. In the CDP model, the plastic strain is defined rather than the total strain and can be calculated as:

$$\varepsilon_c^{pl} = \varepsilon_c - \varepsilon_c^{el} \tag{8}$$

where the compressive damage parameters are not considered [73]. ε_c is the total strain, ε_c^{el} and ε_c^{pl} represent the elastic and plastic strains, respectively.

The post-peak behaviour of the material in tension can be defined by assigning the tensile stress-strain curve, the stress-displacement curve or the stress-fracture energy representing the area under the stress-displacement curve. For a brittle material with little or no reinforcement, the results in the CDP model strongly depend on the mesh size during the crack propagation [80]. After local failures occur, adoption of the tensile stress-strain approach may result in convergence problems even if the mesh refinement is performed [73]. Therefore, the fracture energy in the tension approach was used here. In this study, the tensile strength, f_t , of brick masonry was assumed as $0.035 f_c$ according to previous studies [47,81]. The fracture energy of masonry in tension varies between 0.004 N/mm and 0.055 N/mm in relation to its tensile strength as observed experimentally by various researchers [82–85]. As an empirical approach based on the experimental results [82–85], the following equation was used in the CDP model as:

$$G_t = 0.1\, f_t^{0.85} \tag{9}$$

where the f_t is in N/mm^2 and G_t is in N/mm.

In Abaqus/Explicit, the contact modelling between the structural components can be addressed with two main approaches: general contact and contact pairs (CP) in relation to desired computational efficiency. This study employs the CP approach by defining leading and following surfaces, named as master and slave surfaces in the FE terminology, with tangential and normal stress behaviour of the surfaces in contact referring to the friction and normal pressures, respectively. The default option for normal behaviour is hard contact, whilst the friction coefficient needs to be defined for tangential behaviour with a penalty formulation which is detailed in both the validation and case studies.

Another important issue is the time increment control and associated stability in the explicit scheme. While Abaqus/Standard employs the equilibrium between external and internal forces with the Newton-Raphson iteration method, Abaqus/Explicit integrates the dynamic nodal responses, e.g. velocity, stress, at each time increment. Thus, the stability of the numerical model strongly depends on the time increment which needs to be controlled considering the maximum frequency of all elements [73]. When considering this highly nonlinear dynamic problem, the automatic option for adjusting the time increments in Abaqus/Explicit was used in this present research.

3.2. FEM Validation study: brick masonry parapet walls subject to out-of-plane impact load

Despite various studies conducted on the structural behaviour of masonry arch bridges subject to vertical loads under static or quasi-static loads [58,78,79] and in-plane horizontal loads e.g. from seismic action [86], there are no readily available studies on the behaviour of masonry arch bridges under dynamic horizontal loads in the transverse direction [22]. Hence, an experimental study on masonry parapet walls under out-of-plane impact loads representing accidental vehicle impacts [87] was chosen to examine the capability of the FE modelling approach. Gilbert et al. [87] performed a detailed experimental investigation on the behaviour of unreinforced masonry walls using different wall thickness, wall length, masonry unit type and strength, boundary conditions, impact locations etc. From the test series conducted [87], a free-standing brickwork parapet wall subject to out-of-plane impact load, named as specimen B2 and shown in Fig. 8(a), was chosen to simulate with the FE method. The dimension of the brickwork wall was 9.15 m long x 1.07 m high x 0.215 m wide constructed on a rectangular steel base plate with 0.012 m thickness which was bolted to the floor. The loads were applied at the centre of a steel loading plate with dimensions of 0.4 x 0.4 x 0.05 m where the centre was located 0.555 m above the base of masonry wall. In the experiment, a test rig comprising a drop weight with adjustable drop height was used to obtain different impulse values with various peak impact forces and impact durations. In this present study, the out-of-plane impact load exerted by the 380 kg mass dropped from a 2.5 m height corresponding to a 2.66 kNs impulse load was applied to the wall from the centre of the steel loading plate with the force-time history given in Fig. 8(b).

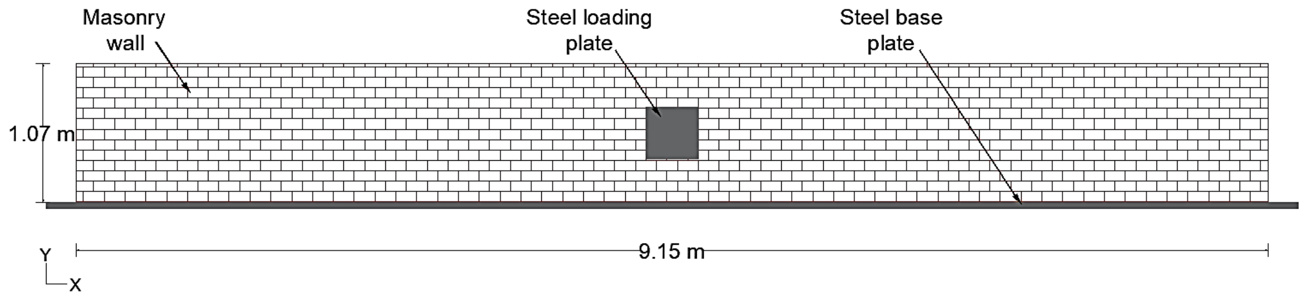

(a) Front elevation view of test arrangement

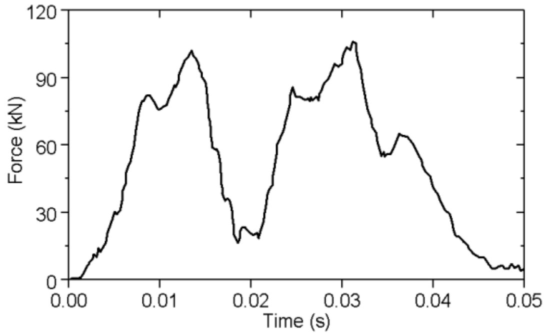

(b) Force-time history

Fig. 8: (a) Front elevation view of the test setup for wall B2, (b) impact force-time history applied at the centre of the steel loading plate (based on [87])

Specimen B2 was constructed from clay bricks of 2200 kg/m^3 density and 134 N/mm^2 compressive strength bonded by mortar type class iii based on BS5628 part 1 [75], with the mean density of 2090 kg/m^3 and compressive strength of 8.6 N/mm^2 were used. Also, the experiment determined the friction coefficient of 0.85 between the steel base plate and the masonry wall [87].

Table 5: Plasticity parameters and mechanical properties of brick masonry in the CDP model

Plasticity parameters				
Dilation angle(ψ)	Eccentricity(ϵ)	f_{b0}/f_{c0}	K_c	Viscosity(μ)
30	0.1	1.16	0.67	0
Mechanical properties of brick masonry				
Density (kg/m^3)	f_c (N/mm^2)	E_c (N/mm^2)	f_t (N/mm^2)	G_t (N/mm)
2150	13.82	7604	0.484	0.054

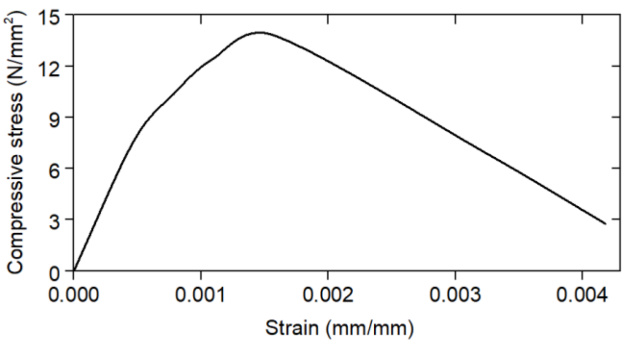

Fig. 9: Compressive stress-strain curve of masonry

To simulate the experiment, the masonry wall and steel loading plate were first modelled with the same dimensions given in the experiment by assuming the loading plate as a rigid body in the FE model. The linear and nonlinear material properties of masonry were defined as provided in Table 5. The default values for the plasticity parameters; ϵ, f_{b0}/f_{c0}, K_c and μ were employed. The dilatation angle, ψ, was chosen based on the previous studies on masonry arch bridges [58,59,70]. The compressive strength of masonry, f_c, was calculated from Eq. 5 using the compressive strengths of brick and mortar provided in the experiment. E_c was obtained according to Eq. 7. Eq. 6 was used to calculate ε_c and the associated compressive stress-strain curve of masonry as illustrated in Fig. 9, where Eq.8 evaluated the plastic strain, ε_c^{pl} for the CDP model by using ε_c and ε_c^{el} values at the descending branch of the curve with the ultimate plastic strain of 0.00359. An f_t of 0.484 N/mm^2 was adopted in the FE model corresponding to $0.035f_c$ as previously discussed. G_t was calculated based on Eq. 9 and the Poisson's ratio of 0.2 was used in all FE models.

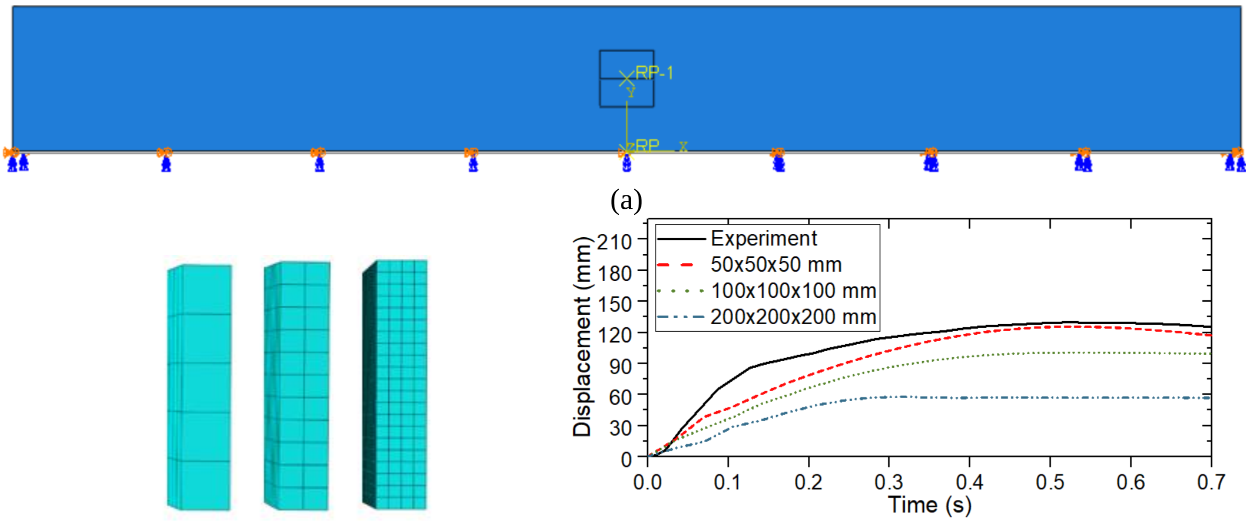

(a)

(b)

(c)

Fig. 10: (a) Front view of FE model with applied boundary conditions (b) side view of FE model with three mesh sizes; coarse, medium, fine and (c) comparison of displacement histories between experiment and FE models using three mesh sizes

Reflecting the experimental boundary conditions, the movements and rotations of the wall were restricted in the x and z directions and the y direction at the base, see Fig. 8(a) and Fig. 10(a). A two-step analysis was performed for the validation study: (1) the first step was the structural analysis of the wall under the dead load, while in the second step (2) the force-time history was applied to the masonry wall through the centre of the steel loading plate using the amplitude option in Abaqus. The CP interaction with a surface-to-surface option was employed between the loading plate and masonry wall by using a friction coefficient of 0.85 in the penalty formulation in the tangential direction as provided in the experiment and hard contact in the normal direction. Considering the simple rectangular geometry of the masonry parapet wall, the *h*-refinement approach was used by defining mesh sizes globally rather than defining local seeds. Fig. 10(b) illustrates a side view of the FE model with three different mesh sizes in relation to the number of the element along the width of the wall: coarse, medium and fine meshes representing approximately 200 x 200 x 200 mm, 100 x 100 x 100 mm and 50 x 50 x 50 mm element sizes, respectively, while Fig. 10(c) compares the displacement histories at 440 mm above the base, 115 mm from the centre of the loading steel beam, between the experiment and the different mesh sized models. It can be observed that there is significant mesh sensitivity in this case and noted that the prediction for the displacement value at 0-0.12 s associated with the first crack could not be improved by refining the mesh size. Hence the finest mesh size was chosen with 3.4% error at the peak displacement and 1.3 s computational (CPU) time where t = 0.7 s was physical time via use of the Intel i7- 10875H CPU @2.30 GHz.

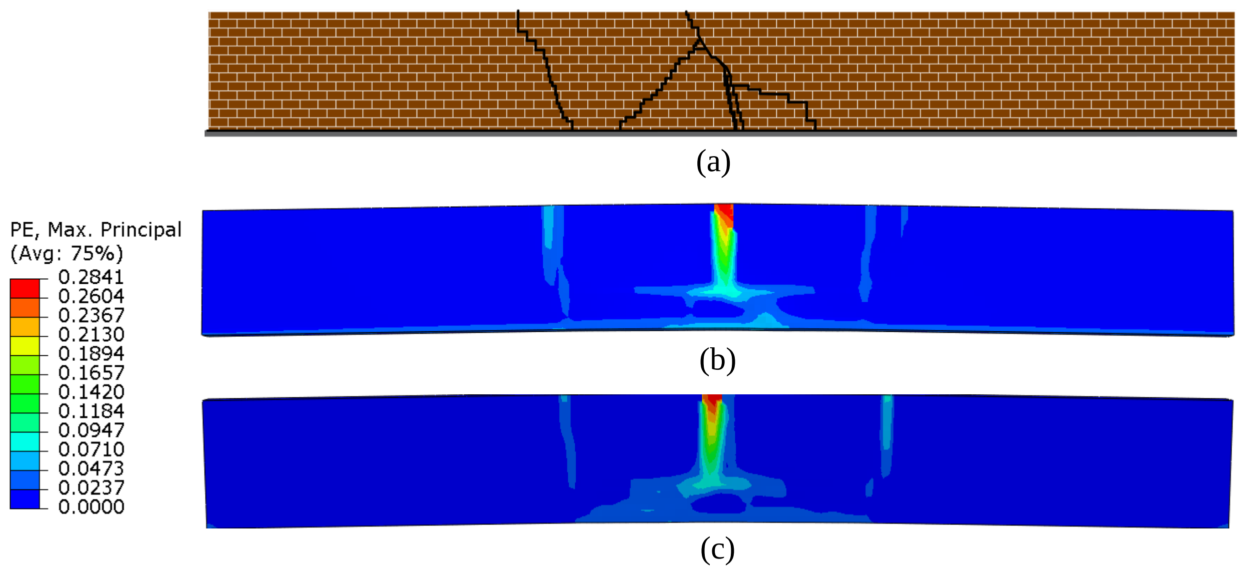

Fig. 11: Comparison between crack patterns on masonry wall B2 (a) experimental based on [87] (b) numerical, front face and (c) numerical, back face of the wall at t = 0.7 s (scale factor = 0.5)

Fig. 11(a) shows the crack pattern of wall B2 at failure obtained in the experiment, whilst Fig. 11(b) and Fig. 11(c) provide the crack pattern at the front and back face of the wall at the end of simulation, $t = 0.7$ s. Considering the crack pattern of wall B2 observed in Fig. 11(a), the FE model could capture the approximate crack pattern reasonably well. Another numerical study in the literature also simulated this experiment using simplified micro-modelling [69]. For further comparison, the displacement history at 440 mm above the base, 115 mm from the centre of the loading steel beam obtained in the FE model was compared with the experimental study and the simplified micro-modelling approach of Burnett et al. [69] as given in Fig.12. The macro-model predicted the peak displacement value well with 3.4% error, in closer agreement with the experimental value than simplified micro-modelling with the 61.3% error. The study of Burnett et al. [69] used a nonlinear constitutive model only for the interfaces via a specially formulated contact interface model, while a linear constitutive model was employed for all other parts including the masonry units. The greater error in the simplified micro-model may be due to the influence of the key contact interface parameters: base friction, fracture energy, dilation angle and joint failure stress according to [69]. It should also be stated that Burnett et al. [69] obtained a closer agreement for other wall cases such as those with abutments compared to wall B2 and their simplified micro-model can undoubtedly provide detailed information for local behaviour of the structure.

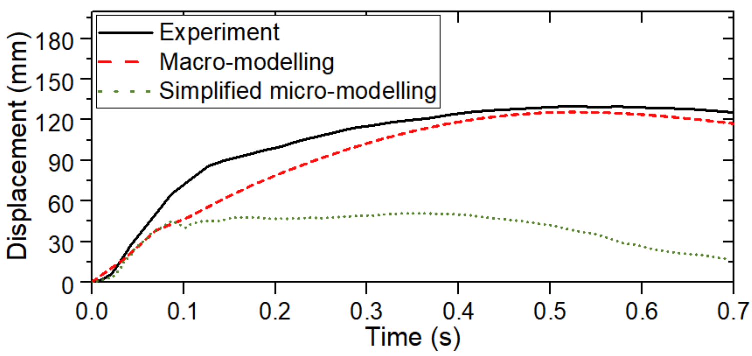

Fig. 12: Comparison of displacement histories [69,87]

3.3. Hydrodynamic case studies

As detailed previously in Table 2, the geometric characteristics of a representative full-scale single-span masonry arch bridge was used in this study with 0.25 rise-to-span ratio, 0.45 m thick arch barrel, 0.55 m thick spandrel wall and 0.3 m backfill depth above the crown.

Table 6: Mechanical properties of brick masonry

Density (kg/m^3)	f_c (N/mm^2)	E_c (N/mm^2)	f_t (N/mm^2)	G_t (N/mm)
2000	9.33	5132	0.33	0.039

The material properties of the masonry arch barrel and spandrel wall used in this study are summarised in Table 6. The f_c of 9.33 N/mm^2 was used based on an experimental study in the literature [49], E_c , f_t and G_t were defined following the same procedures as the validation study. The CDP parameters were the same as the validation study, whilst the compressive stress-strain behaviour of brick masonry was calibrated based on the f_c value and ε_c as seen in Fig. 13. The present study assumed the masonry arch bridge is waterproof and therefore does not include any saturation in the backfill, thus the density of 1800 kg/m^3 and E_c of 100 N/mm^2 were used for backfill modelling based on [58,70].

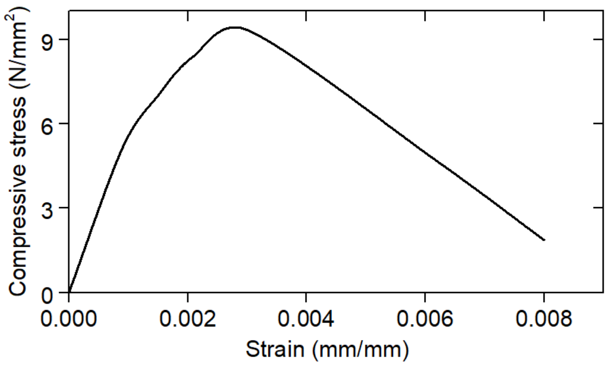

Fig. 13: Compressive stress-strain curve of brick masonry

Following the validation study, CP interaction was employed between the arch barrel, front and back spandrel walls and backfill defining normal behaviour with a hard contact option and tangential behaviour with a penalty option. In the penalty formulation, a friction coefficient of 0.85 was used between the masonry arch barrel and spandrel walls, while a value of 0.3 was used between the backfill and the masonry members such as the arch barrel and spandrel walls in accordance with the friction angle of the backfill material based on previous numerical studies

[58,70]. The same element type, C3D8R, with the validation study was used in the case studies. To optimise model resolution, a mesh sensitivity analysis was performed using various mesh sizes for structural components. The global mesh sizes of approximately 100 mm and 50 mm were employed for the spandrel wall and arch barrel, respectively, whilst an adaptive mesh refinement technique was performed using various mesh sizes locally by means of creating partitions and local seeds so as to apply the debris impact on represented elements as well as to tackle convergence problems in relation to meshing the complex arch barrel and spandrel wall geometry, see Fig. 14(a) for case 1. The mesh size for backfill was kept relatively coarser with element sizes around ~ 200 mm to optimise the computational efficiency.

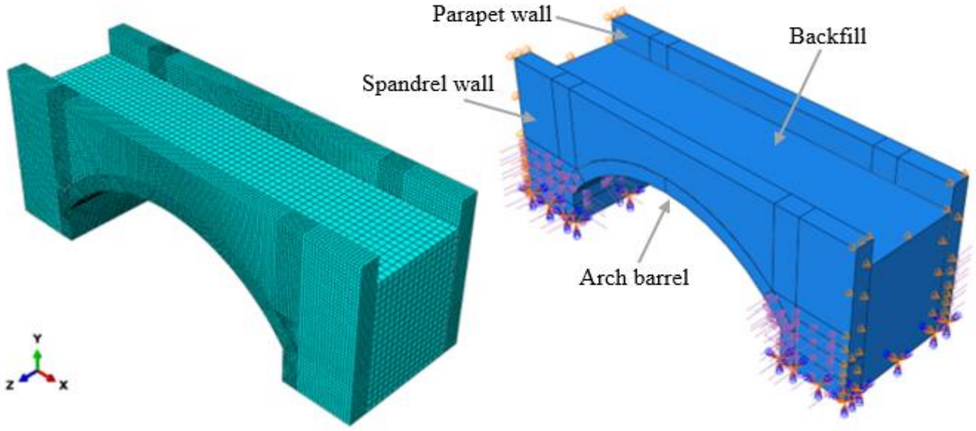

(a) (b)

Fig. 14: (a) Mesh, (b) boundary conditions and loads applied in case 1

The boundary conditions were fixed at the bottom of the bridge with no displacement in the *x*, *y* and *z* directions and no displacement in the *x* direction was defined at the sides of the spandrel wall and backfill considering previous numerical studies [60,70]. Similar to the validation study, the dead loads and flood-induced loads were applied at the first step and second step of the analysis, respectively. As previously described, for the input loads, the pressure values obtained from the SPH models, see Fig. 4, were multiplied by 10 in accordance with Froude scaling and applied to associated areas via use of partition in Abaqus as shown in Fig. 14(b). To apply the debris impact pressure-time histories at the same location as the hydrodynamic simulations, the pressure probe spacing used in the SPH model and in the FE model were the same. For these purposes, the mesh sizes were kept spatially uniform at the location where the debris impacted. It should be reiterated that although the geometrical similarity between the prototype and model was provided successfully, the dynamic similarity, thus kinematic similarity, was constrained by the flume capacity used in the experiment. The free-surface velocity of the flow was 0.2 m/s in the experiments with all submergence ratios representing a velocity of 0.63 m/s the full-scale scenario. Field data from real life flood scenarios reveal much faster flows can occur e.g. 3.14 m/s at Pooley Bridge, 3.2 m/s at Eamont Bridge, 4.2 m/s at Brougham Bridge and 4.3 m/s at Sprint Bridge during the 2015 UK flood events as detailed previously in Table 1. In view of this, the pressure-time histories obtained using corresponding higher flow velocities [88] were also used to investigate associated structural response to these loads as detailed in Section 3.3.3.

3.3.1. Results: hydrodynamic loads only in slow flow (v_{flow} = 0.63 m/s)

Three scenarios were examined where the following structural components were submerged: abutment in case 1, arch barrel in case 2 and spandrel wall in case 3, respectively, see Table 3 and Fig. 4. The bridge was subject to dead load only before applying the flood-induced loads as an initial step (Fig.15(a)). Fig. 15(b), Fig. 15(c) and Fig. 15(d) show the maximum principal stress distribution on the bridge in case 1, case 2 and case 3 where the stress values are presented in N/mm^2. As can be seen from the results, the hydrodynamic effect on the bridge was relatively small due to using lower free-surface velocity values compared to typical values from real flooding scenarios. Although the dominant loading was the hydrostatic pressure in these cases increasing with the water depth from the free surface to the bottom of the bridge in all cases, higher tensile stress values occurred where the arch barrel and spandrel wall were submerged in case 2 and case 3. The significant effect of buoyancy and reduction in the compressive stress state of the barrel can be clearly observed from Fig. 15(a) to Fig. 15(d). The maximum tensile stress on the arch barrel was around 0.172 N/mm^2 in case 2, while this value was ~0.187 N/mm^2 in case 3 where the tensile strength of the masonry is 0.33 N/mm^2. Nevertheless, the tensile stresses are significant especially given the range of tensile strengths expected in the field.

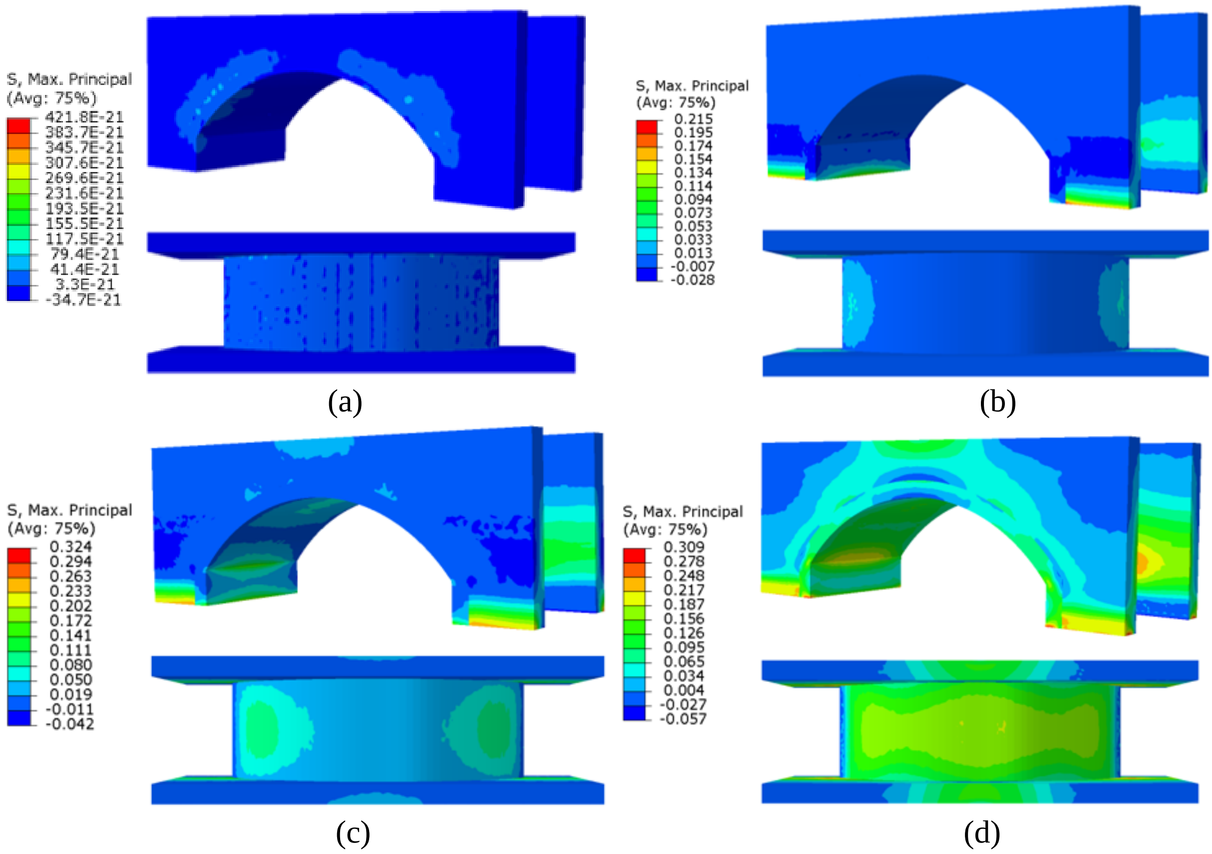

Fig. 15: Maximum principal stress distribution on masonry arch bridge under (a) only dead load, (b) hydrodynamic load in case 1, (c) case 2 and (d) case 3 at the end of simulation corresponding to t =10 (N/mm^2) with front and top views

3.3.2. Results: combination of hydrodynamic and debris impact loads in slow flow (v_{flow} = 0.63 m/s)

Fig. 16 illustrates the maximum tensile stress distribution on the bridge under the combination of hydrodynamic and debris impact loads in case 1A at t = 6.4 s where only the abutment was submerged, see Fig. 4(b), Fig. 4(c), Fig. 5(c) and Fig. 5(d). Compared to case 1, the presence of the debris resulted in increasing the overall stress distribution slightly with 2.33 percent higher maximum tensile stress, 0.22 N/mm^2, while the tensile stress values on the arch barrel and spandrel walls were 1.57 times higher (157%) in case 1A compared with those in case 1. Despite lower tensile stress values in the cases with the free-surface velocity of 0.63 m/s, this floating debris impact load directly links to the debris velocity associated with the free-surface velocity of the water flow.

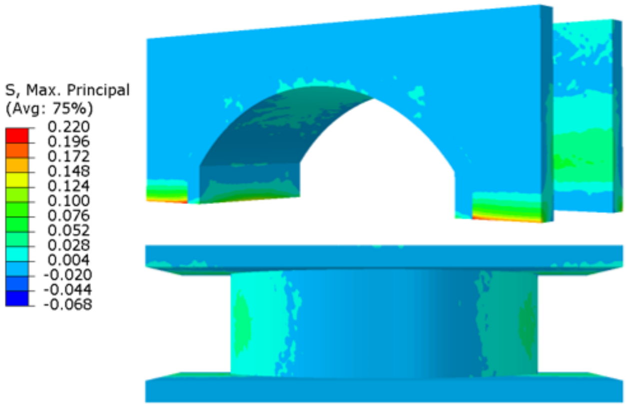

Fig. 16: Maximum principal stress distribution on masonry arch bridge in case 1A at t = 6.4 s (N/mm^2)

Fig. 17(a) and Fig. 17(b) give the maximum tensile stress distribution on the masonry arch bridge with a fully submerged arch barrel in case 2A and case 2B corresponding to 0-degree and 90-degree debris impacts, respectively. Although 8 times higher debris impact pressures were applied to the structure within ~0.2 s impact duration in case 2B, the associated stress distribution cannot be distinguished in Fig. 17(b) and the overall ~3% increment was observed in the tensile stresses on the arch barrel and spandrel walls in the case 2A and case 2B. This might be due to relatively slow debris velocity associated with lower free-surface velocity with the submerged arch barrel in both case 2A and case 2B as well as the short impact duration in case 2B despite its higher pressure values. Similarly with case 2A and case 2B, a slight change in the response of the bridge was observed in case 3A and case 3B compared to case 3 as shown in Fig. 17(c) and Fig. 17(d). It can be concluded that the floating debris impact loads and associated response of the bridge under these loads are strongly dependent on the free-surface velocity. Fig. 16 and Fig. 17(a)-(d) show that when the submergence ratio of the bridge increases, the velocity of the free surface decreases, thus the debris impact loads and its effect on the bridge descrease, and hence the debris impact loads and their effect on the bridge descrease. Another important issue is the debris impact duration. While the debris impact with 90-degree orientation resulted in 8 times higher load exerted on the bridge in case 2B compared to case 2A and 1.53 times higher in case 3B compared to case 3A, the response of the bridge to these higher loading conditions with shorter impact duration within ~0.2–0.3 s is almost the same, in terms of the resulting stresses, with the cases with 0-degree debris orientations.

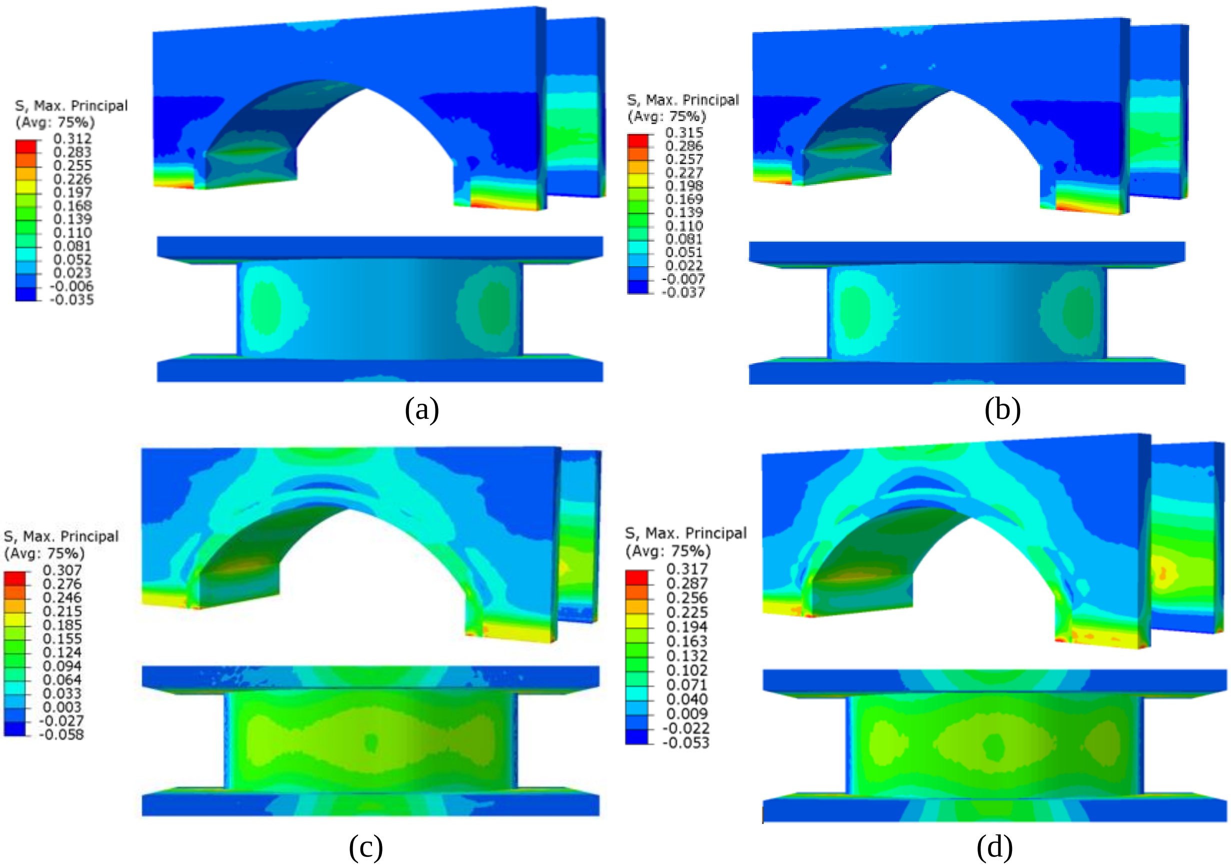

Fig. 17: Maximum principal stress distribution on masonry arch bridge (N/mm^2) in (a) case 2A at t = 8.6 s , (b) case 2B at t = 6.4 s, (c) case 3A at t = 10 s and (b) case 3B at t = 8.5 s

3.3.3. Real-life flooding scenario with only hydrodynamic loads (v_{flow} = 3.14 m/s)

The flow velocity in rivers varies depending on the topographical and hydrological conditions where the river flow interacts with the masonry arch bridge. Considering hydraulic reports at the location of the Pooley Bridge collapse due to the flood in Cumbria, UK during the 2015 flood event (Table 1), the mean velocity reached 3.14 m/s around the bridges as detailed by Environment Agency and Mathews and Hardman [8,16] . Despite detailed investigation needed to examine these flood-induced loads on Pooley Bridge, this section provides a general estimation of how flood-induced loads may cause bridge damage or collapse using the same representative bridge and higher flow velocity value of 3.14 m/s observed during the real-life flooding compared to 0.63 m/s used in the previous case study which was based on the experimental setup.

Following the case study, the 1:10 scaled bridge model was used for SPH simulations. For the hydraulic conditions, the case of the fully submerged arch barrel was adopted with the mean model-scale velocity of 1 m/s so as to represent ~3.14 m/s in the full-scale as detailed by Majtan et al. [88]. The structural response of the full-scale masonry arch bridge under this flooding scenario was examined in FE using the same boundary conditions and interaction properties among the structural components as the case study.

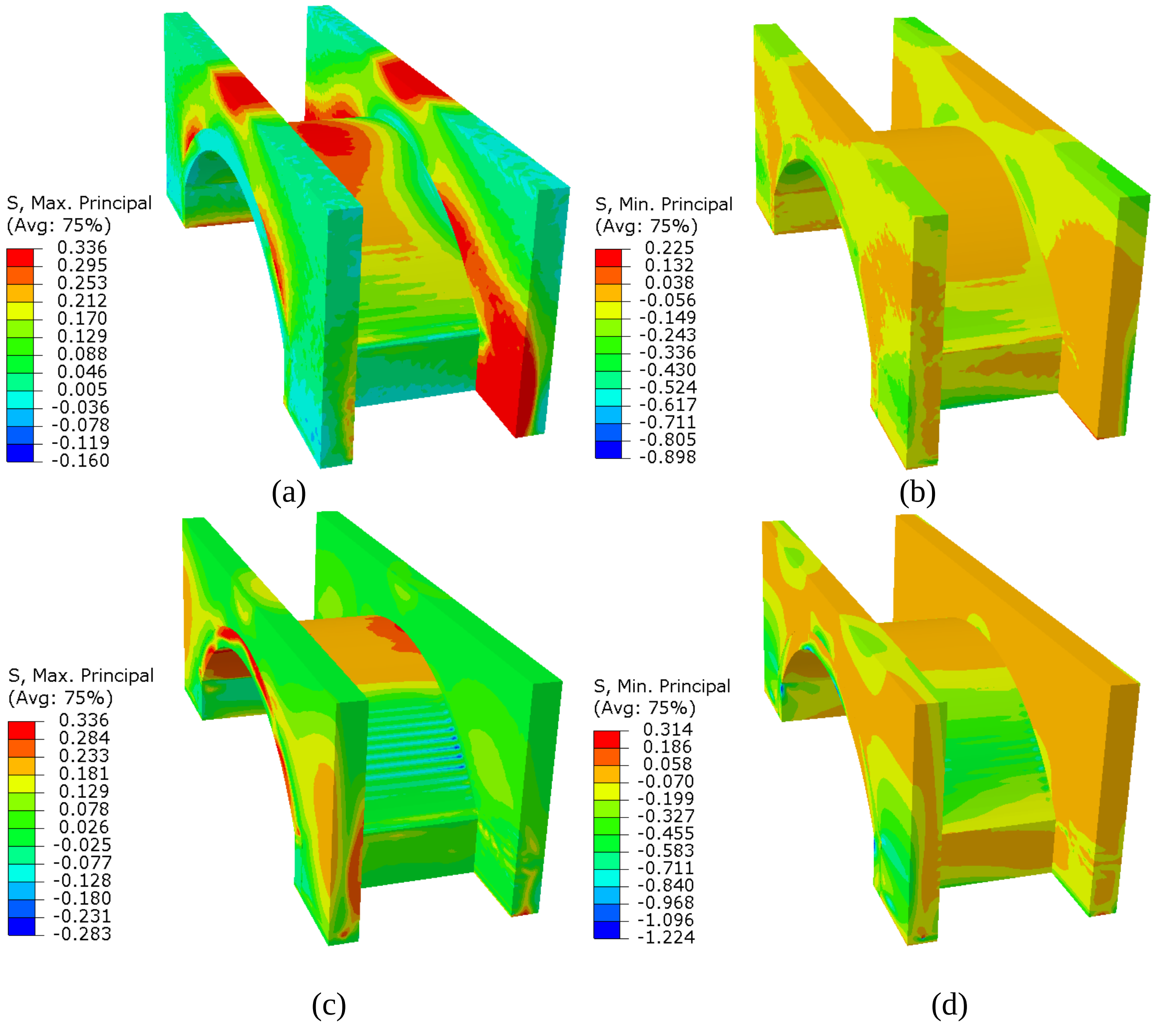

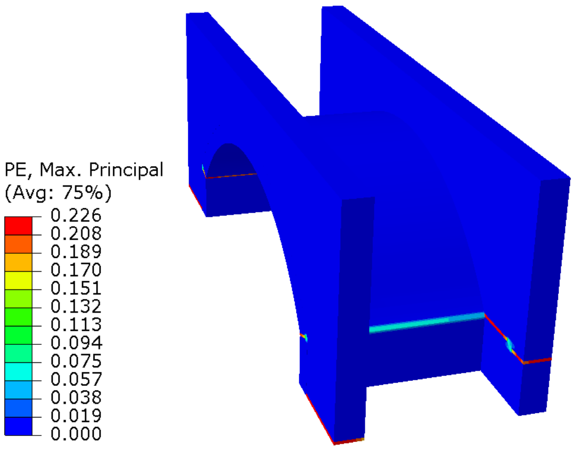

(e)

Fig. 18: Flooding scenario with fully submerged arch barrel, (a) maximum principal stress distribution and (b) minimum principal stress distribution on the bridge during the first crack, (c) maximum principal stress distribution, (d) minimum principal stress distribution and (e) crack patterns at the end of simulation

Fig. 18(a) shows the maximum tensile stress distribution at the first time-step, 0.2 s in the FE. The maximum stress reached the tensile strength of 0.33 N/mm^2 on the spandrel wall and arch barrel rather than the bottom of the abutment compared to the case 2 with dominant hydrostatic loads, therefore the material failure was observed at the first time-step. After this material failure, the tensile stresses tend to zero with increasing strain as the maximum tensile stress distribution and crack pattern on the bridge at the end of simulation are given in Fig 18(c) and Fig. 18(e), respectively. Meanwhile, the minimum stresses show that no compressive failure occurred during the first crack, at 0.2 s Fig. 18(b) and at the end of the simulation Fig. 18(d).

4. Conclusions

In this paper, flood-induced hydrostatic, hydrodynamic and floating debris pressures on a representative masonry arch bridge were derived using the SPH method. These pressure-time histories were then used to model the associated structural response of the bridge using the FEM. The adopted macro modelling approach was first validated against existing experimental work on brick masonry parapets subject to impact. A good level of accuracy was achieved in terms of the displacement vs. time response and associated crack patterns in comparison with the experimental results. The main findings of this investigation reveal that:

- Increase in the submergence ratio of a waterproof bridge led to higher tensile stress development on the bridge superstructure due the buoyancy effect.
- Impacts from floating woody debris, even in normal, non-flood scenarios, can result in significant impulsive forces. Depending on the location of the impact, local damage may arise in the form of cracking, this in turn can lead to progressive damage via secondary mechanisms such as fill washout etc.
- Debris with an initial orientation of 90-degrees (end-on) to the bridge span exerted larger forces compared to the 0-degree (side-on) scenario with a fully submerged arch barrel and spandrel. However, these forces had very short durations and hence the resulting tensile stresses in the arch components were only slightly greater than those associated with the hydrodynamic forces alone i.e. in the absence of debris.
- A realistic flood flow, based on data from previous flood events, indicated that the hydrodynamic load was the fundamental driver in bridge damage. The maximum tensile stresses were observed at the spandrel wall and arch barrel, leading to crack developed and structural damage.

This work reveals that both the hydrodynamic forces and floating debris impact forces need to be considered when assessing existing masonry arch bridges that span watercourses. Quantification of these associated flood forces can lead to improved bridge management strategies to ensure these structures continue to perform in service. The outcomes of this work need to be viewed within the context of the limitations of the SPH and FE methodologies adopted. Further work is required to refine the FE models, including more detailed modelling of the backfill soil, associated effects from water ingress due to cracking of the masonry as well as the effect of pre-existing defects in the bridge structure.

Declaration of competing interests

The authors declare that they have no known competing financial interests or personal relationships that could have appeared to influence the work reported in this paper.

Acknowledgements

This work was founded by the Ministry of National Education of the Republic of Turkey. The authors are grateful to Dr Adrian Bell and Dr Kurdo F. Abdulla for their helpful conversations on masonry structures and Research IT at the University of Manchester for their assistance on the use of Computational Shared Facility.

References

[1] Orbán Z. UIC Project on assessment , inspection and maintenance of masonry arch railway bridges. 5th Int Conf Arch Bridg 2007:3–12.
[2] Proske D, Hubl J. Historical arch bridges under horizontal loads 2006;100.
[3] Jonkman S. Loss of Life Due to Floods: General Overview. Drowning, Berlin, Heidelberg: Springer Berlin Heidelberg; 2014, p. 957–65. https://doi.org/10.1007/978-3-642-04253-9_148.
[4] Deng L, Wang W, Yu Y. State-of-the-art review on the causes and mechanisms of bridge collapse. J Perform Constr Facil ASCE 2016;30:04015005. https://doi.org/10.1061/(ASCE)CF.1943-5509.0000731.
[5] Rowson J, Wynne A. Cumbrian bridges ripped out by torrential floods. New Civ Eng 2009:6–7.
[6] Lynch D. Cumbria gets stuck into bridge repairs. New Civ Eng 2010:10–1.
[7] BBC. Storm Christoph: “18 months” for plans to repair Llanerch bridge 2021. https://www.bbc.co.uk/news/uk-wales-55807741 (accessed September 21, 2021).
[8] Environment Agency, Cumbria County Council. Pooley Bridge Flood Investigation Report. 2016.
[9] Environment Agency, Cumbria County Council. High and Low Lorton Flood Investigation Report. 2016. https://doi.org/10.1093/nq/s5-II.30.75-a.
[10] Jecock M, Jessop L. Tadcaster Bridge , Tadcaster , North Yorkshire : Assessment of Significance. 2016.
[11] Mott Macdonald, Cumbria County Council. Bridge by bridge. 2018.
[12] DfI, TEO, DCSDC. North west flooding review. 2018.
[13] BBC. Cumbria floods resulted in £276m bill 2010. https://www.bbc.co.uk/news/uk-england-cumbria-11791716 (accessed September 21, 2021).
[14] Cumbria County Council. Braithwaite Section 19 Flood Investigation Report. 2017.
[15] BBC. Storm Desmond-destroyed historic Bell Bridge replaced 2017. https://www.bbc.co.uk/news/uk-england-cumbria-42417486 (accessed September 21, 2021).
[16] Mathews R, Hardman M. Lessons learnt from the December 2015 flood event in Cumbria, UK. Proc Inst Civ Eng Forensic Eng 2017;170:165–78. https://doi.org/10.1680/jfoen.17.00009.
[17] Bill Harvey Associates Limited. 125. Merry Harriers 2021. http://www.billharveyassociates.com/bom/125-merry-harriers (accessed September 21, 2021).
[18] The Institution of Structural Engineers. Brougham Castle Bridge 2018. https://www.istructe.org/structuralawards/previously-shortlisted/structural-heritage/2018/brougham-castle-bridge (accessed September 21, 2021).
[19] Institution of Civil Engineers. The repair of Tadcaster Bridge . 2018 n.d. https://www.ice.org.uk/what-is-civil-engineering/what-do-civil-engineers-do/the-repair-of-tadcaster-bridge (accessed September 21, 2021).
[20] North Yorkshire County Council. Yorkshire Dales reconnected thanks to bridge reopening

2021. https://www.northyorks.gov.uk/news/article/yorkshire-dales-reconnected-thanks-bridge-reopening (accessed September 21, 2021).
[21] Ebrahimi M, Kripakaran P, Djordjević S, Tabor G, Kahraman R, Prodanović DM, et al. Hydrodynamic effects of debris blockage and scour on masonry bridges: Towards experimental modelling. Scour Eros - Proc 8th Int Conf Scour Erosion, ICSE 2016 2016:743–50. https://doi.org/10.1201/9781315375045-93.
[22] Proske D, Krawtschuk A, Zeman O, Scheidl C, Chiari M. Debris flow impacts on masonry arch bridges. Proc Inst Civ Eng Bridg Eng 2018;171:25–36. https://doi.org/10.1680/jbren.16.00005.
[23] National Highways. BD 97/12 : The assessment of scour and other hydraulic actions at highway structures. vol. 3. 2012.
[24] Takano H, Pooley M. New UK guidance on hydraulic actions on highway structures and bridges. Proc Inst Civ Eng Bridg Eng 2021;174:231–8. https://doi.org/10.1680/jbren.20.00024.
[25] Ciria. Manual on Scour at Bridges and Other Hydraulic Structures (C742). London, UK: 2017.
[26] National Highways. CD 356: Design of highway structures for hydraulic action. 2020.
[27] National Cooperative Highway Research Program (NCHRP) Report 445. Debris Forces on Highway Bridges. Washington, the US: 2000.
[28] Hulet KM, Smith CC, Gilbert M. Load-Carrying Capacity of Flooded Masonry Arch Bridges. Proc ICE-Bridge Eng 2006;159:97–103. https://doi.org/10.1680/bren.2006.159.3.97.
[29] Kindij A, Ivanković AM, Vasilj M. Adjustment of small-span masonry arch bridges to present-day demands. J Croat Assoc Civ Eng 2014. https://doi.org/10.14256/jce.972.2013.
[30] Huang W, Xiao H. Numerical Modeling of Dynamic Wave Force Acting on Escambia Bay Bridge Deck during Hurricane Ivan. J Waterw Port, Coastal, Ocean Eng 2009;135:164–75. https://doi.org/10.1061/(asce)0733-950x(2009)135:4(164).
[31] Hartana, Murakami K, Yamaguchi Y, Maki D. 2-Phase Flow Analysis of Tsunami Forces Acting on Bridge Structures. J Japan Soc Civ Eng Ser B3 (Ocean Eng 2013;69:I_347-I_352. https://doi.org/10.2208/jscejoe.69.i_347.
[32] Chu C-R, Chung C-H, Wu T-R, Wang C-Y. Numerical Analysis of Free Surface Flow over a Submerged Rectangular Bridge Deck. J Hydraul Eng 2016;142:1–11. https://doi.org/10.1061/(ASCE)HY.1943-7900.0001177.
[33] Ebrahimi M, Kahraman R, Kripakaran P, Djordjević S, Tabor G, Prodanović DM., et al. Scour and hydrodynamic effects of debris blockage at masonry bridges: insights from experimental and numerical modelling 2017.
[34] Shadloo MS, Oger G, Le Touzé D. Smoothed particle hydrodynamics method for fluid flows, towards industrial applications: Motivations, current state, and challenges. Comput Fluids 2016;136:11–34. https://doi.org/10.1016/J.COMPFLUID.2016.05.029.
[35] Violeau D, Rogers BD. Smoothed particle hydrodynamics (SPH) for free-surface flows: past, present and future. J Hydraul Res 2016;54:1–26. https://doi.org/10.1080/00221686.2015.1119209.
[36] Gomez-Gesteira M, Rogers BD, Dalrymple RA, Crespo AJC. State-of-the-art of classical SPH for free-surface flows. J Hydraul Res 2010;48:6–27. https://doi.org/10.1080/00221686.2010.9641242.
[37] Khayyer A, Gotoh H, Falahaty H, Shimizu Y. An enhanced ISPH–SPH coupled method for simulation of incompressible fluid–elastic structure interactions. Comput Phys Commun 2018;232:139–64. https://doi.org/10.1016/j.cpc.2018.05.012.
[38] Hasanpour A, Istrati D, Buckle I. Coupled sph–fem modeling of tsunami-borne large debris flow and impact on coastal structures. J Mar Sci Eng 2021;9. https://doi.org/10.3390/jmse9101068.

[39] Capasso S, Tagliafierro B, Martínez-Estévez I, Domínguez JM, Crespo AJC, Viccione G. A DEM approach for simulating flexible beam elements with the Project Chrono core module in DualSPHysics. Comput Part Mech 2022. https://doi.org/10.1007/s40571-021-00451-9.
[40] Hermange C, Oger G, Le Chenadec Y, Le Touzé D. A 3D SPH–FE coupling for FSI problems and its application to tire hydroplaning simulations on rough ground. Comput Methods Appl Mech Eng 2019;355:558–90. https://doi.org/10.1016/j.cma.2019.06.033.
[41] Sarhosis V, De Santis S, de Felice G. A review of experimental investigations and assessment methods for masonry arch bridges. Struct Infrastruct Eng 2016;12:1439–64. https://doi.org/10.1080/15732479.2015.1136655.
[42] Sarhosis V, Forgács T, Lemos J V. A discrete approach for modelling backfill material in masonry arch bridges. Comput Struct 2019;224:106108. https://doi.org/10.1016/j.compstruc.2019.106108.
[43] Forgács T, Sarhosis V, Ádány S. Shakedown and dynamic behaviour of masonry arch railway bridges. Eng Struct 2021;228. https://doi.org/10.1016/j.engstruct.2020.111474.
[44] Crespo AJC, Domínguez JM, Rogers BD, Gómez-Gesteira M, Longshaw S, Canelas R, et al. DualSPHysics: Open-source parallel CFD solver based on Smoothed Particle Hydrodynamics (SPH). Comput Phys Commun 2015;187:204–16. https://doi.org/10.1016/j.cpc.2014.10.004.
[45] Domínguez JM, Fourtakas G, Altomare C, Canelas RB, Tafuni A, García-Feal O, et al. DualSPHysics: from fluid dynamics to multiphysics problems. Comput Part Mech 2021 2021:1–29. https://doi.org/10.1007/S40571-021-00404-2.
[46] Majtan E, Cunningham LS, Rogers BD. Experimental and numerical investigation of floating large woody debris impact on a masonry arch bridge. J Mar Sci Eng 2022;10:1–21. https://doi.org/https://doi.org/10.3390/jmse1007091.
[47] Cavaleri L, Ciraolo G, Ferrotto MF, La Loggia G, Lo Re C, Manno G. Masonry structures subjected to tsunami loads: Modeling issues and application to a case study. Structures 2020;27:2192–207. https://doi.org/10.1016/j.istruc.2020.08.033.
[48] Knudtsen JA, Kabele P, Biggs DT. Modelling a masonry arch bridge - comparing methods. J Int Mason Soc Mason Int 2019;32:1–19.
[49] Hendry AW. Masonry properties for assessing arch bridges. 1990.
[50] Jansen L, Korswagen PA, Bricker JD, Pasterkamp S, de Bruijn KM, Jonkman SN. Experimental determination of pressure coefficients for flood loading of walls of Dutch terraced houses. Eng Struct 2020;216:110647. https://doi.org/10.1016/j.engstruct.2020.110647.
[51] Majtan E, Cunningham LS, Rogers BD. Flood-induced Hydrodynamic and Debris Impact Forces on Single-span Masonry Arch Bridge. J Hydraul Eng 2021;147. https://doi.org/DOI: 10.1061/(ASCE)HY.1943-7900.0001932.
[52] Dalrymple R, Rogers B. Numerical modeling of water waves with the SPH method. Coast Eng 2006;53:141–7.
[53] Chow AD, Rogers BD, Lind SJ, Stansby PK. Incompressible SPH (ISPH) with fast Poisson solver on a GPU. Comput Phys Commun 2018;226:81–103. https://doi.org/10.1016/J.CPC.2018.01.005.
[54] Monaghan JJ. Simulating free surface flows with SPH. J Comput Phys 1994;110:399–406. https://doi.org/10.1006/jcph.1994.1034.
[55] Barreiro A, Crespo AJC, Domínguez JM, Gómez-Gesteira M. Smoothed Particle Hydrodynamics for coastal engineering problems. Comput Struct 2013;120:96–106. https://doi.org/10.1016/j.compstruc.2013.02.010.
[56] Pringgana G, Cunningham LS, Rogers BD. Modelling of tsunami-induced bore and structure interaction. Proc Inst Civ Eng Eng Comput Mech 2016;169:109–25. https://doi.org/10.1680/jencm.15.00020.

[57] Tafuni A, Domínguez JM, Vacondio R, Crespo AJC. A versatile algorithm for the treatment of open boundary conditions in Smoothed particle hydrodynamics GPU models. Comput Methods Appl Mech Eng 2018;342:604–24. https://doi.org/10.1016/j.cma.2018.08.004.

[58] Boothby TE, Roberts BJ. Transverse behaviour of masonry arch bridges. Struct Eng 2001;79:21–6.

[59] Fanning PJ, Boothby TE, Roberts BJ. Longitudinal and transverse effects in masonry arch assessment. Constr Build Mater 2001;15:51–60. https://doi.org/10.1016/S0950-0618(00)00069-6.

[60] Kamiński T. Tests to collapse of masonry arch bridges simulated by means of FEM. Proc. 5th Int. Conf. Bridg. Maintenance, Saf. Manag., 2010, p. 1431–8. https://doi.org/10.1201/b10430-206.

[61] Gibbons N, Fanning PJ. Rationalising assessment approaches for masonry arch bridges. Proc Inst Civ Eng Bridg Eng 2012;165:169–84. https://doi.org/10.1680/bren.11.00023.

[62] Zevenbergen LW, Lagasse PF, Clopper PE. Effects of debris on bridge pier scour. Restoring Our Nat. Habitat - Proc. 2007 World Environ. Water Resour. Congr., 2007. https://doi.org/10.1061/40927(243)376.

[63] Ebrahimi M, Kripakaran P, Prodanović DM, Kahraman R, Riella M, Tabor G, et al. Experimental Study on Scour at a Sharp-Nose Bridge Pier with Debris Blockage. J Hydraul Eng 2018;144:04018071. https://doi.org/10.1061/(asce)hy.1943-7900.0001516.

[64] Magilligan FJ, Nislow KH, Fisher GB, Wright J, Mackey G, Laser M. The geomorphic function and characteristics of large woody debris in low gradient rivers, coastal Maine, USA. Geomorphology 2008;97:467–82. https://doi.org/10.1016/j.geomorph.2007.08.016.

[65] BS EN 338. Structural timber - strength classes. Br Stand Inst 2016.

[66] Moreno EC. Wave energy conversion based on multi-mode line absorbing systems. University of Manchester, 2015.

[67] Abdulla KF, Cunningham LS, Gillie M. Simulating masonry wall behaviour using a simplified micro-model approach. Eng Struct 2017;151:349–65. https://doi.org/10.1016/j.engstruct.2017.08.021.

[68] Yacila J, Camata G, Salsavilca J, Tarque N. Pushover analysis of confined masonry walls using a 3D macro-modelling approach. Eng Struct 2019;201:109731. https://doi.org/10.1016/j.engstruct.2019.109731.

[69] Burnett S, Gilbert M, Molyneaux T, Beattie G, Hobbs B. The performance of unreinforced masonry walls subjected to low-velocity impacts: Finite element analysis. Int J Impact Eng 2007;34:1433–50. https://doi.org/10.1016/j.ijimpeng.2006.08.004.

[70] Kamiński T. Three-dimensional modelling of masonry arch bridges based on predetermined planes of weakness. Proceeding 5th Int. Conf. Arch Bridg. - ARCH'07, Madeira, Portugal: 2007.

[71] Zhang Y, Tubaldi E, Macorini L, Izzuddin BA. Mesoscale partitioned modelling of masonry bridges allowing for arch-backfill interaction. Constr Build Mater 2018;173:820–42. https://doi.org/10.1016/j.conbuildmat.2018.03.272.

[72] Wahalathantri BL, Thambiratman D, Chan T, Fawzia S. A Material Model for Flexural Crack Simulation in Reinforced Concrete Elements Using ABAQUS. Proc. First Int. Conf. Eng. Des. Dev. Built Environ. Sustain. Wellbeing, 2011, p. 260–4.

[73] Abaqus. Abaqus 6.14 Documentation. 2014.

[74] Michał S, Andrzej W. Calibration of the CDP model parameters in Abaqus. 2015world Congr Adv Struct Eng Mech 2015:1–11.

[75] BSI. BS 5628: Code of practice for use of masonry. 1978.

[76] BSI. EN 1996-1-1:2005 Eurocode 6: Design of masonry structures - Part 1-1: General rules for reinforced and unreinforced masonry structures. London: 2005.

[77] Kaushik HB, Rai DC, Jain SK. Stress-Strain Characteristics of Clay Brick Masonry under

Uniaxial Compression. J Mater Civ Eng 2007;19:728–39. https://doi.org/10.1061/(ASCE)0899-1561(2007)19:9(728).
[78] Page J. Load Tests To Collapse on Two Arch Bridges At Preston, Shropshire and Prestwood, Staffordshire. Res Rep - Transp Road Res Lab 1987.
[79] Page J. Load tests to collapse on two arch bridges at Torksey and Shinafoot. Res Rep - Transp Road Res Lab 1988.
[80] Abdulla KF. Innovative strengthening techniques for adobe masonry structures. 2019.
[81] Schubert. P. The influence of mortar on the strength of masonry. In: Courcy IJW de, editor. 8th Int. Brick Block Mason. Conf, 1988, p. 162–74.
[82] Ganz H., Thürlimann B. Tests on masonry walls under normal and shear loadingThurman - Google Search. ETH Zurich, Switzerland: 1984.
[83] Pluijm van der R. Non-Linear Behaviour of Masonry under Tension. Pluijm, Rob van Der 1997;42:25–54.
[84] Beattie G. Joint fracture in reinforced and unreinforced masonry under quasi-static and dynamic loading. Dep Civ Eng 2003.
[85] Da Porto F, Guidi G, Garbin E, Modena C. In-Plane Behavior of Clay Masonry Walls: Experimental Testing and Finite-Element Modeling. J Struct Eng 2010;136:1379–92. https://doi.org/10.1061/(asce)st.1943-541x.0000236.
[86] Pelà L, Aprile A, Benedetti A. Seismic assessment of masonry arch bridges. Eng Struct 2009;31:1777–88. https://doi.org/10.1016/j.engstruct.2009.02.012.
[87] Gilbert M, Hobbs B, Molyneaux TCK. The performance of unreinforced masonry walls subjected to low-velocity impacts: experiments. Int J Impact Eng 2002;27:231–51. https://doi.org/10.1016/j.ijimpeng.2006.08.004.
[88] Majtan E, Cunningham LS, Rogers BD. Investigation of flood forces on masonry arch bridges using SPH. In: Mike Forde, editor. Proc. 18th Eur. Bridg. Conf., 2022, p. 1–11. https://doi.org/0-947644-89-X.